@driptadutta

Dripta Dutta || Takeshi Imayama || Dyuti Prakash Sarkar || Kaushik Das

Creep behaviours of omphacite and amphibole-plagioclase symplectite: The role of heterogeneous hydration in the Tso Morari eclogite during retrogression

Dripta Dutta[1]*, Takeshi Imayama[1], Dyuti Prakash Sarkar[2,#], Jun-ichi Ando[2], Kaushik Das[2]

[1] Institute of Frontier Science and Technology, Okayama University of Science, Okayama 700-0005, Japan

[2] Department of Earth and Planetary Systems Science, Hiroshima University, Higashi Hiroshima 739-8526, Japan

[#] now at Division of Earth Sciences, Graduate School of Sciences and Technology for Innovation, Yamaguchi University, Yoshida 753-8512, Japan

* Correspondence - dutta-dripta@ous.ac.jp, dripta.dutta@gmail.com (Dripta Dutta)

ORCiD - 0000-0001-9247-6388 (DD), 0000-0002-7704-4963 (Takeshi Imayama), 0000-0001-7406-5956 (Dyuti Prakash Sarkar), 0000-0002-2372-2095 (Kaushik Das)

Abstract

Replacement reactions progress to varying degrees depending on the P-T conditions, exhumation rates, and fluid availability. The collective preservation of the reactants and partly to completely retrogressed products allows reconstruction of the microstructural and mineralogical progression, which we investigated using electron backscattered diffraction and microprobe analyses on the omphacite, amphibole-plagioclase symplectite, and matrix amphibole of the Tso Morari eclogite. The elliptical shapes, absence of chemical zonation, and scarce subgrains suggest that the omphacite deformed via body diffusion creep. Because of the heterogeneous distribution of hydrous fluids in the eclogite, the omphacite is replaced by amphibole-plagioclase symplectite either partially along the peripheries (S1 symplectite) or completely (S2 symplectite). Strong omphacite CPOs, caused by growth anisotropy, are inherited by the symplectite constituents such that $\langle 001 \rangle_{Omp}//\langle 001 \rangle_{Amp}//\langle 010 \rangle_{Plag}$, $\langle 010 \rangle_{Omp}//\langle 010 \rangle_{Amp}$, and $\langle 100 \rangle_{Omp}//\langle 100 \rangle_{Amp}//\langle 001 \rangle_{Plag}$. The amphiboles in S1 are poorer in Si (6.75–7.34 apfu) and crystallised earlier than those in S2 (Si = 7.29–7.79 apfu) during retrogression. Elevated stresses at the reaction interfaces deformed the plagioclase in S1 via dislocation creep. In contrast, the plagioclase in S2 deformed via grain boundary diffusion creep accommodated grain boundary sliding due to fluid abundance. The misorientations across the subgrain boundaries in the amphibole grains constituting S1 and S2 are similar to those in the amphibole of the eclogite matrix and the garnet amphibolites. The amphibole in S1, eclogite matrix, and garnet amphibolites deformed via dislocation creep, whereas dislocation creep accommodated grain boundary sliding deformed those in S2. *(239 words)*

Keywords *- CPO Inheritance, Deformation mechanism, Growth anisotropy, Dislocation creep, Diffusion creep, Dissolution-precipitation, Grain Boundary Sliding*

1. Introduction

The exhumation velocity and its temporal variations, in addition to the pressure-temperature trajectory and fluid availability, greatly influence the textural features preserved in exhumed lithounits. Fast and near-isothermal decompression of UHP units enables them to record disequilibrium textures, which were generated by the incomplete reactions or transformations during the rapidly varying P-T conditions and are represented by the presence of the reactant(s) in contact with the products (Mørk 1985; Wayte et al. 1989; García-Casco and Torres-Roldán 1996; Peterman and Grove 2010; Gaidies et al. 2017; Ogilvie and Gibson 2017). Symplectite complexes exemplify such coexistence between the products and the reactant. They are typically characterised by a complex and vermicular intergrowth of two or more secondary phases, which crystallised simultaneously due to the destabilisation of a primary phase caused by the changing pressure and/or temperature conditions (Spry 1969; Barker 1998). The omphacite in exhumed UHP eclogites, upon decompression, generally disintegrates to diopside-plagioclase symplectite, which gradually transforms into amphibole-plagioclase aggregate due to retrogression in the presence of hydrous fluids (Martin and Duchêne 2015; Martin 2019). Partial breakdown of omphacite to amphibole-plagioclase symplectite due to late-stage hydrous fluid influx has also been observed (Massonne 2012). The textural attributes of their intergrowth, such as lamellar or granular, correlate with slow and fast exhumation, respectively (Anderson and Moecher 2007). The lamellar spacing in diopside-plagioclase symplectite can also be used to estimate temperatures (Joanny et al. 1991). Most importantly, symplectitisation involves the inheritance of the crystallographic preferred orientations (CPOs) of the precursor parent phase by the daughter crystals (Heidelbach and Terry 2013; Spruzeniece et al. 2017a; Zertani et al. 2024).

Deformation experiments have demonstrated that a diopside-plagioclase aggregate is plastically weaker than pure clinopyroxene (Dimanov and Dresen 2005). Hydration and amphibole formation can further lower the bulk plastic strength of the aggregate (Marti et al. 2018). Thus, symplectitisation, which also involves grain size reduction, should naturally result in the rheological weakening of eclogites (Jamtveit et al. 2016; Zertani et al. 2024). A recent CPO study shows that the symplectite constituents in the UHP eclogite of the Western Gneiss Region (Norway) deformed via grain size-sensitive (GSS) creep (Zertani et al. 2024). Nevertheless, Mansard *et al.* (2020) performed deformation experiments to demonstrate that the absence of interconnected layers of fine-grained reaction products could inhibit or impede bulk rock weakening. Although the reaction-induced decrease in the grain size and consequent switch to GSS creep is predicted to be more efficient during retrogression (Brodie and Rutter 1987), it is not impossible for the products of positively dilatant transformation reactions to experience intracrystalline plastic deformation via dislocations (Greenwood and Johnson 1965; White and Knipe 1978; Poirier 1982, 1985).

Despite the interrelationships between metamorphism and deformation, previous workers assessed either the geochemical (O'Brien 1993; Brodie 1995; Martin 2019) or the microstructural (Odashima et al. 2007; Heidelbach and Terry 2013; Spruzeniece et al. 2017a; Zertani et al. 2024) attributes of symplectite. Consequently, the mechanisms facilitating the deformation of the symplectitic minerals at the initial and final stages of their growth in naturally deformed eclogites remain poorly understood. This contribution examines one eclogite and two garnet amphibolites from the Tso Morari region. In the eclogite, we investigated the deformation characteristics of the Na-rich clinopyroxene and the symplectitic minerals, which either partially or completely replaced the former. We have further integrated the compositional and textural features of the symplectitic amphiboles to reconstruct their sequential development and deformation. The crystallographic preferred orientations and mineral chemistries of the symplectitic amphiboles are also compared with those in the eclogite matrix and the garnet amphibolites to discern the characteristic variations with retrogression. Our inferences are based on thin section petrography, electron microprobe data, and electron backscattered diffraction study.

2. Geological Setting

The Tso Morari Crystallines (TMC) is a part of the Indian Trans-Himalaya. It lies to the immediate south of the Indus Tsangpo suture zone (Fig. 1a). Structurally, the TMC is a northwesterly trending antiformal dome and forms the footwall of the detachment faults that separate it from the surrounding lithounits, i.e., Nidar Ophiolite in the north and Tetragoal Nappe in the south (de Sigoyer et al. 2004; Buchs and Epard 2019) (Fig. 1b). The variably deformed granite gneiss, also known as the Tso Morari Gneiss or the Puga Gneiss, contain boudinaged metabasite (retrograded eclogite and garnet amphibolite) layers that occur nearly parallel to the gneissic foliations. The eclogite units within the TMC are proposed to be derived from either the Permian basalt of the Panjal Traps (Spencer et al. 1995; Jonnalagadda et al. 2019) or the Early Cretaceous Ladakh ophiolites (Ahmad et al. 2022). Recently, Imayama et al. (2024) used trace element geochemistry and U-Pb geochronology to demonstrate that Early Paleozoic bimodal and multi-stage magmatism, in a continental rift setting, produced the protoliths of the TMC gneiss and metabasite. Epard and Steck (2008) also reported undeformed granitic bodies separating the metabasite boudins and postulated the cogenetic origin of the felsic and mafic protoliths. The protolith to the eclogite boulder (17-6C, Fig. 1a) from the north of the Zildat Shear Zone could have been an island-arc basalt instead (Imayama et al. 2024). Previous studies have identified mineral assemblages corresponding to the prograde path (e.g., St-Onge et al., 2013), eclogite-facies peak metamorphism (de Sigoyer et al. 1997; Wilke et al. 2015; Palin et al. 2017; Pan et al. 2020; Dey et al. 2023), granulite facies thermal peak (St-Onge et al. 2013; Chatterjee and Jagoutz 2015), and amphibolite-facies retrogression (Mukherjee et al. 2003; Chatterjee and Jagoutz 2015) from the metabasites. The corresponding P-T conditions estimated by the authors are listed in Table ST1 in Supplementary File S1. The metamorphic evolution of the metabasites is extensively studied and, therefore, numerous P-T paths have been proposed, which suggest that the TMC rocks subducted to at least 70 km of depth, experienced a thermal maximum during the nearly isothermal decompression, and exhumed along a higher geothermal gradient after the peak temperature. Although the metamorphic history of the felsic component of the TMC is relatively less investigated, textural evidence of peak-pressure metamorphism in the eclogite facies is present (Guillot et al. 1997; Bidgood et al. 2023), including the quartz after coesite pseudomorph in the unstrained Early Ordovician granite exposed near Polokongka La (Bidgood et al. 2021), which is also reported to be the protolith of the Tso Morari Gneiss (Girard and Bussy 1999). Epard and Steck (2008) identified four deformation phases from the Tso Morari Gneiss and the overlying nappes, all related to their extrusion, i.e., occurred after the peak pressure eclogite facies metamorphism. They have also reported that oriented relics of omphacite in the eclogite are rare and, therefore, proposed that the eclogite facies or UHP deformation was weak and characterised by static recrystallisation of omphacite. In contrast, de Sigoyer et al. (1997, 2004) proposed that the peak pressure deformation (2.3 GPa and 580 ± 60 °C) at ~ 55 Ma caused the omphacite in the eclogite to recrystallise dynamically and develop the preferred alignment.

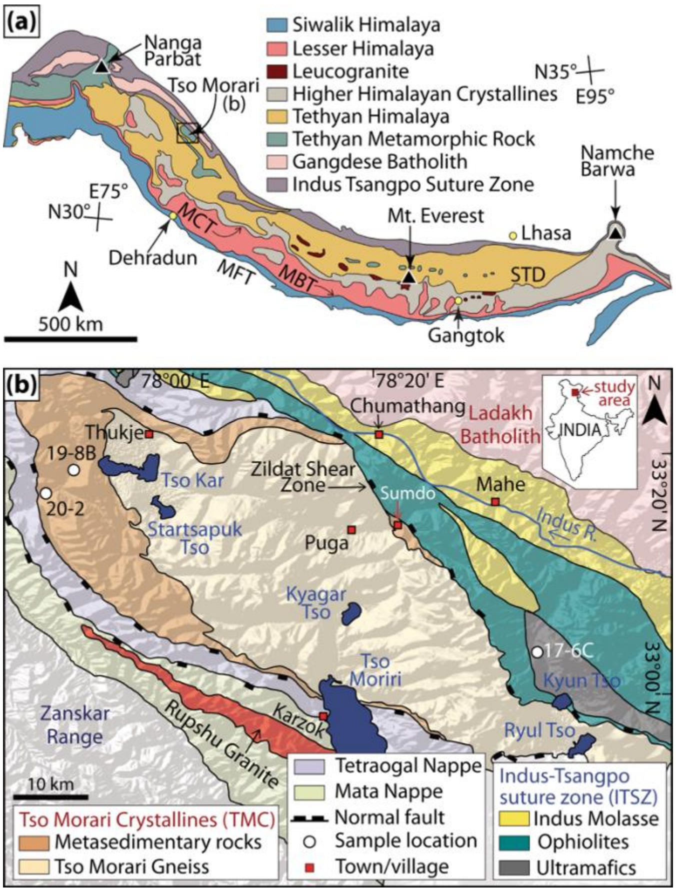

Fig. 1 *Geological maps of the study area.* ***(a)*** *Geological map of the Himalayan orogen (reproduced from Dutta and Mukherjee, 2021). The yellow circles mark the locations of major cities/towns. The black triangles mark the major mountain peaks. The black unfilled square demarcates the study area.* ***(b)*** *Geological map of the Tso Morari region (redrawn after de Sigoyer et al., 2004 and Epard and Steck, 2008).*

3. Analytical methods

Three non-oriented samples, 17-6C, 19-8B, and 20-2, are studied (Fig. 1b). Sample 17-6C is an eclogite (fig. SF1 in the Supplementary File S1) collected from the north of the Zildat Shear Zone. The garnet amphibolite samples 19-8B and 20-2 are collected from within the metasedimentary sequence that mantles the Tso Morari Gneiss. Samples 17-6C and 19-8B are non-foliated and, therefore, sliced along random directions to prepare the thin sections, whereas the weakly foliated sample 20-2 lacks clear lineation and, therefore, is cut along the dip direction and perpendicular to the foliation. The thin sections are used for petrography and electron microprobe analysis. Rock chips (1.3 cm × 1.3 cm in area and 0.5 cm thick), one each from samples 17-6C, 20-2, and 19-8B, are sliced using the Buehler IsoMet Low-Speed Saw. Struers 0.25 μm diamond paste is used for the final polishing of the thin sections and the rock chips. The analysed surfaces of the rock chips of samples 19-8B and 20-2 are parallel to their respective thin sections. The rock chips are used for backscattered electron imaging, electron microprobe analysis, and electron backscattered diffraction (EBSD) study.

3.1 Thin section petrography and backscattered electron imaging

The thin sections are used to perform the preliminary petrographic study with a polarizing microscope. Backscattered electron (BSE) images are acquired from the rock chips using the JEOL JXA-8230 electron probe microanalyzer at the Okayama University of Science, Japan. For BSE imaging, the working distance, beam current, and acceleration voltage are set to 11mm, 12 nA, and 15 kV, respectively. The rock chips were carbon-coated before BSE imaging and electron microprobe analysis.

3.2 Electron microprobe analysis

Mineral chemistry data are obtained from the thin sections and the rock chips using the JEOL JXA-8230 electron probe microanalyzer at the Okayama University of Science, Japan. The rock chips are mainly used to determine the mineral chemistries of the grains present at the exact locations mapped using the EBSD (Sec. 3.3). The working conditions are the same as those used during BSE imaging. We used a beam spot size of 3 μm for the measurements. Routine analytical calibration is performed using natural and synthetic samples of the following silicates and oxides. Oxides of nine elements – Si, Al, Ti, Fe, Mn, Mg, Ca, Na, and K – are measured in wavelength dispersive X-ray spectrometry modes by acquiring the following X-ray lines – Si$K\alpha$, Al$K\alpha$, Ti$K\alpha$, Fe$K\alpha$, Mn$K\alpha$, Mg$K\alpha$, Ca$K\alpha$, Na$K\alpha$, and K$K\alpha$. The ZAF correction algorithm is followed to perform the matrix corrections. An X-ray map is also acquired from the thin section of sample 17-6C to check whether the omphacite are zoned. The Al, Ca, Fe, Mg, Na, and Si intensities for omphacite and symplectite in the map are simultaneously measured with a 15 kV accelerating voltage and a 25 nA beam current.

Mineral chemistries of the amphibole in the eclogite matrix are studied from the rock chips. The amphibole and plagioclase constituting the symplectite and the adjacent coarser clinopyroxene are targeted in the thin section and the chips of 17-6C. In 19-8B and 20-2, mineral chemistries of the amphibole are analysed from the respective rock chips. The clinopyroxene structural formula is normalized to four cations and six oxygens. For amphibole, the normalization assumes that the M4 site does not contain Mg, Fe, or Mn, and Si + Al + Ti + Mg + Fe + Mn = 13 (Stout 1972; Droop 1987). The plagioclase structural formula is recalculated based on eight oxygens.

3.3 Electron backscattered diffraction (EBSD) study

The EBSD data are acquired from the rock chips. Final polishing of the chips is carried out for four hours with 0.05 μm colloidal silica suspension using a vibratory polisher, following which they are coated with Osmium. EBSD mapping is carried out at the Department of Earth and Planetary Systems Science, Hiroshima University, Japan, using JEOL JSM-6390A SEM, equipped with a Nordlys EBSD detector and the AZtec software package (Oxford Instruments), at an accelerating voltage of 15 kV, working distance of 22 mm, pattern acquisition time of 96–146 ms, and a sample tilt of 70°.

EBSD mapping is performed in five regions (Sites 1S, 1S-A, 2S, 5M, and 7M) of the eclogite sample 17-6C (fig. SF2 in Supplementary File S1). Site 1S is the largest among them. It contains multiple coarse clinopyroxene grains with similarly oriented long axes, which are mainly targeted for EBSD and, therefore, it is mapped using a step size of 3 μm. Two EBSD maps target the symplectite regions – Sites 1S-A (lies within Site 1) and 2S, targeting the symplectite categories S1 and S2 (discussed in Sec. 4.1.1), respectively. Sites 1S-A and 2S have smaller areas than Site 1S and are mapped at 1 μm step size. The symplectite regions are selected from locations that contain fewer or are located near the clinopyroxene grains with their long axes oriented nearly parallel to those in Site 1S. Site 5M focuses mainly on the matrix amphibole adjacent to a garnet porphyroblast. It is also mapped at a step size of 2 μm. A coarse quartz (Site 7M) from the eclogite matrix is mapped using a step size of 1 μm to better detect the intragranular orientation variations. An amphibole-rich region is mapped from the garnet amphibolite sample 19-8B at a step size of 3 μm. In sample 20-2, we mapped two adjacent regions composed mainly of elongated amphibole using step sizes of 2 μm. These regions are stitched together using the HKL Channel 5 Map Stitcher software package. The garnet amphibolites are included in the study to examine the differences in the texture, composition, and deformation mechanisms between their amphibole and those constituting the symplectite and the matrix in the eclogite. Some fine-grained clinopyroxenes in the symplectites are Ca-rich (diopsidic) (Table ST2 in the Supplementary File S1). They could not be indexed as a clinopyroxene phase separate from that of the more dominant Na-rich clinopyroxene during the EBSD mapping. Since the finer clinopyroxene is scarce in the symplectite and because this work focuses on the Na-rich clinopyroxene instead, we removed all the finer clinopyroxene from the symplectites while processing the EBSD data and did not analyse them further.

The raw EBSD data are post-processed using the MTEX toolbox 5.10.2 (Hielscher and Schaeben 2008) on a MATLAB 2024b platform. Cleaning the raw data during post-processing included discarding poorly indexed pixels, i.e., those with mean angular deviations

>1.5° and grains composed of less than five pixels. Grain reconstruction is performed using the Voronoi decomposition algorithm in MTEX (Bachmann et al. 2011). 10° is chosen as the threshold misorientation angle to define the grain boundaries. All Dauphine twin boundaries in quartz are also merged. The orientation distribution functions used to plot the pole figures are calculated using a de la Vallée Poussin kernel halfwidth of 10°. The pole figures for the symplectite regions are presented as lower hemisphere projections on equal-area nets using orientation data from all the indexed pixels, which are coloured as per the orientation colouring scheme (IPF key) of the corresponding mineral to ease the visual inspection of the orientation relationships between the grains of different phases. We use the one-point-per-grain scheme to plot the rest of the pole figures. They are contoured if there are at least 50 grains. The strengths of the crystallographic preferred orientations (CPOs) are reported only for those that are contoured using the misorientation index (Skemer et al. 2005).

The EBSD data are also used to generate misorientation angle distributions (MADs) of neighbouring and randomly selected grain pairs. Intragranular or low-angle (2 to <10º) misorientation axis distributions are plotted for minerals only when their grains exhibit visible subgrain boundaries longer than 5 pixels. Maps illustrating the relative misorientation of each pixel within a grain to the mean orientation of the grain (mis2mean) are also generated to determine the extent of intragranular plastic deformation. For easier visualization, separate mis2mean maps are constructed for omphacite, amphibole, plagioclase, and quartz. Misorientation profiles, both point-to-point and cumulative (point-to-origin), are also constructed, following the MTEX-based script of Sikdar *et al.* (2023), along line segments within selected grains of omphacite, amphibole, plagioclase, and quartz to quantify the misorientations across the subgrain boundaries.

4. Results

4.1 Petrography

4.1.1 Sample 17-6C

The eclogite consists of garnet, omphacite, amphibole, quartz, phengite, carbonate minerals, rutile and zoisite. The garnet porphyroblasts preserve the euhedral shapes, and their diameters range from 0.04 to 3 mm (Fig. 2a). Most of the porphyroblasts contain microfractures filled with amphibole, white mica, with or without quartz (fig. SF3a in Supplementary File S1). The omphacite is coarse, with equivalent grain diameters ranging between 0.1 mm and 0.6 mm. They have elliptical outlines with aspect ratios between 2 and 28. They occur as clusters and mostly in the vicinity of the garnet porphyroblasts. Within each cluster, the omphacite exhibits a strong shape-preferred orientation (Fig. 2b,c). Some omphacite grains contain transgranular microfractures characterized by parallel walls, minor dilation, and negligible shear displacement parallel to the walls (Fig. 2c,d), most of which (not all of them) are filled with symplectites. (Fig. 2c,d). The quartz in the matrix exhibit conspicuous subgrain boundaries and fluid inclusion trails (Fig. 2e,f). Although the quartz-quartz boundaries are generally curved, with evident grain boundary migration (Fig. 2f), some are much straighter (fig. SF3b in Supplementary File S1) and probably belong to a remnant vein, as evident from the blocky nature of the quartz grains (fig. SF3b in Supplementary File S1). Prismatic amphibole grains (mapped for EBSD data in Site 5M) occur at boundaries of the garnet porphyroblasts (Fig. 2c) and away from them, with the latter being coarser (Fig. 2g). Coarse white mica is also present in the matrix (Fig. 2h).

The eclogite contains abundant symplectite. These are characterized by the granular intergrowths of amphibole and plagioclase, sometimes together with fine clinopyroxene grains. Depending upon the extent and nature of omphacite replacement, three kinds of symplectite occurrences are observed in the eclogite – (i) partial replacement of the omphacite only along their peripheries (S1) (Fig. 2c,d), (ii) partial replacement along narrow zones across the omphacite (Fig. 2h), and (iii) complete replacement (S2) with (Fig. 2j) or without (Fig. 2k) preserving the precursor grain shape. Some of the coarser amphibole grains in S1 have their long axes perpendicular to the adjacent omphacite boundary (fig. SF3c in Supplementary File S1). The amphibole grains in S2 are coarser at the peripheries than those towards the cores of the omphacite (Fig. 2j). Similarly, in the case of symplectites occupying narrow zones across omphacite, the amphibole grainsizes decrease towards the omphacite interfaces. (Fig. 2l). The coarser amphibole grains in all the symplectites are also relatively more euhedral than the finer ones (Fig. 2i–l).

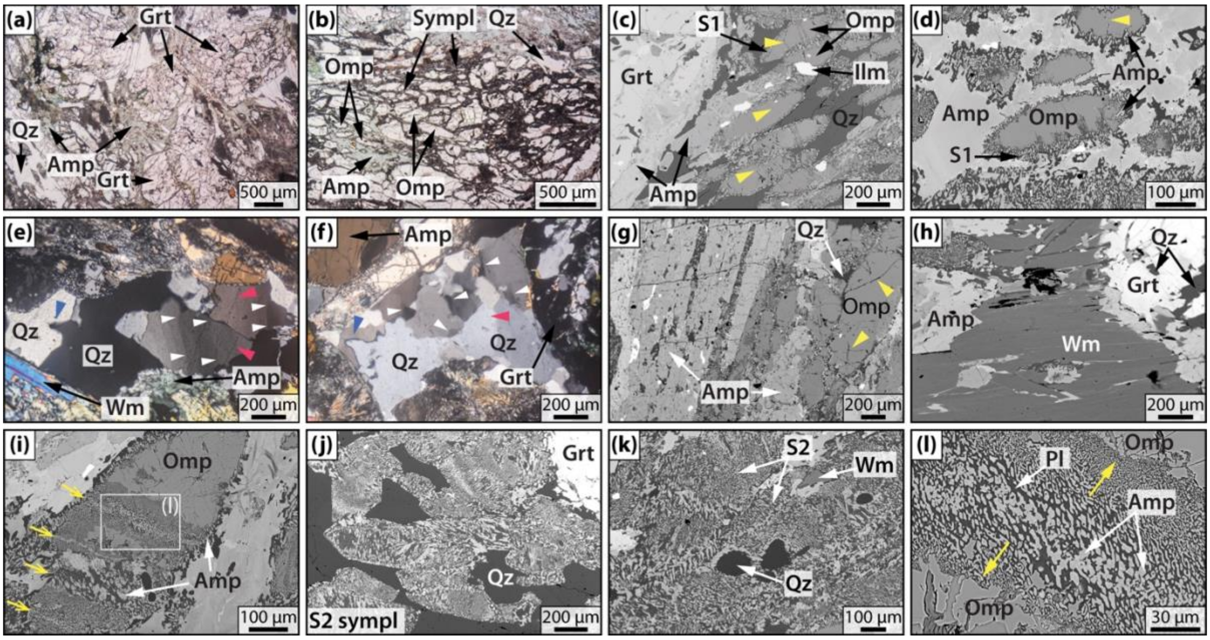

Fig. 2. *Transmitted light photomicrographs and BSE images from the eclogite sample 17-6C.* ***(a)*** *Euhedral garnet porphyroblasts along with quartz and amphibole grains in the matrix (plane-polarized light).* ***(b)*** *Preferentially aligned, elliptical omphacite grains surrounded by symplectitic regions and matrix amphibole (plane-polarized light).* ***(c)*** *Omphacite grains in a matrix of quartz grains near a garnet porphyroblast in the eclogite. Retrograde amphibole grains are also present at the margin of the garnet porphyroblast. The omphacite grains are surrounded by symplectites (type S1), and most of them are fractured (yellow arrowheads).* ***(d)*** *Islands of partly symplectitised (type S1) omphacite within the amphibole matrix.* ***(e,f)*** *Cross-polarized photomicrographs of deformed quartz in the matrix with prominent subgrain boundaries (white arrowheads) and fluid inclusion trails (pink arrowheads). Migrated grain boundaries (blue arrowheads) are also visible.* ***(g)*** *Coarse and prismatic amphibole beside omphacite.* ***(h)*** *Coarse grains of white mica in the matrix alongside amphibole and garnet porphyroblast, with the latter containing inclusions of quartz.* ***(i)*** *Symplectitisation along the periphery of and across the omphacite grain. The thick bands of symplectite are nearly perpendicular to the long axis of the omphacite grains. The thinner linear stripes of coarse amphibole grains marked with the yellow arrows likely represent the original position of the*

fractures along which symplectitisation initiated. ***(j)*** *The shapes of the former omphacite grains are preserved despite their complete replacement by symplectite (type S2).* ***(k)*** *Pervasive symplectitisation (type S2) with little trace of the precursor omphacite grains.* ***(l)*** *Zoomed-in image of* ***(i)*** *illustrating the gradual decrease in the amphibole grainsizes (yellow arrows) away from the initial position of the fracture. Mineral abbreviations are after Whitney and Evans (2010). The yellow arrowheads in* ***(c), (d),*** *and* ***(g)*** *point to the fractures.*

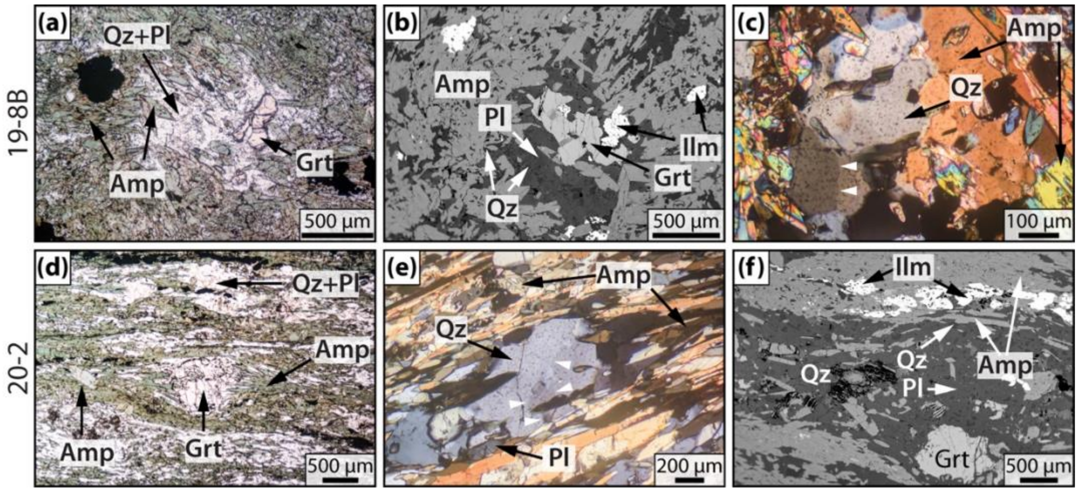

Fig. 3. *Transmitted light photomicrographs and BSE images of the garnet amphibolites.* ***(a)*** *Elongate amphibole grains surrounding a plagioclase-rich domain containing a fragment of a garnet porphyroblast.* ***(b)*** *An isolated patch of quartz-bearing plagioclase-rich domains containing garnet porphyroblasts.* ***(c)*** *Cross-polarized photomicrograph of a deformed quartz grain with a prominent subgrain boundary (white arrowheads) surrounded by amphibole grains.* ***(d)*** *Prismatic amphibole grains define the foliation that warps around the garnet porphyroblast at the center (plane-polarized light).* ***(e)*** *Cross-polarized photomicrograph of a deformed quartz grain with visible subgrain boundaries (white arrowheads).* ***(f)*** *Amphibole-rich layers separated by quartz-bearing plagioclase-rich layers.* ***(a-c)*** *Sample 19-8B.* ***(d-f)*** *Sample 20-2.*

4.1.2 Sample 19-8B

The garnet amphibolite is characterised by the mineral assemblage amphibole, plagioclase, garnet, quartz, ilmenite, and titanite. The plagioclase and quartz occur as isolated patches surrounded by amphibole (Fig. 3a,b). Subgrain boundary is present in some coarser quartz (Fig. 3c). Garnet porphyroblasts as well as ilmenite and titanite grains are more abundant than in sample 20-2 (Fig. 3a).

4.1.3 Sample 20-2

The overall mineral assemblage is same as that of sample 19-8B and the amphibole grains are euhedral and prismatic. They exhibit a strong shape-preferred orientation such their overall arrangement defines the foliation, which is often deflected around the garnet porphyroblasts and, at some places, around the eye-shaped domains of plagioclase feldspar and quartz (Fig. 3d). Most of the quartz grains are finer than the amphibole grains and their long axes are oriented parallel to the foliation. Some of the coarser ones exhibit subgrain boundaries (Fig. 3e), though not as prominent as those in the eclogite matrix. The amphibole-rich layers are separated by those of euhedral and granular plagioclase feldspar and quartz, with the former being much more abundant than the latter (Fig. 3f). The garnet porphyroblasts are present in both amphibole-rich and plagioclase-rich layers. The coarser ones occur in the latter (Fig. 3f), whereas those in the amphibole-rich layers are relatively smaller.

4.2 Mineral chemistry

4.2.1 Eclogite (sample 17-6C)

The coarse and elliptical clinopyroxene grains are Ca-Na clinopyroxene in composition (Table ST2 in Supplementary File S1). The Na contents of these grains lie within 0.53–0.57 apfu and they plot in the omphacite field of the clinopyroxene classification diagram of Morimoto (1989) (fig. SF4a in Supplementary File S1). Ca-rich clinopyroxenes are very few. They are fine-grained and occur within the symplectite. Two such grains are analysed. They are diopside in composition with Na contents of 0.18 and 0.25 apfu (fig. SF4b in Supplementary File S1). The plagioclase in the symplectite is albite to oligoclase ($Ab_{88.8–99.3}$ $An_{0.6–10.5}$ $Or_{0.1–0.7}$) (fig. SF4c and Table ST3 in Supplementary File S1).

The amphibole in the eclogite exhibits a wide range of compositions (Table ST4 in Supplementary File S1). Those in the matrix (Amp-M) mostly plot in the Tschermakite field of the $^{C}(Al+Fe^{3+}+2Ti)$ vs. $^{A}(2Ca+Na+K)$ classification diagram of Hawthorne et al. (2012) (Fig. 4a). The $^{A}(2Ca+Na+K)$ and $^{C}(Al+Fe^{3+}+2Ti)$ contents lie within 0.14–0.70 apfu and 1.36–2.48 apfu, respectively. Their Si contents and $Mg/(Mg+Fe^{2+})$ ratios range between 5.70–6.97 apfu and 0.62–0.97 (Fig. 4b). The ^{B}Na and ^{T}Al contents of these matrix amphibole range from 0.46–0.89 apfu and 1.03–2.30 apfu, respectively (Fig. 4c). Their $^{C}(Al+Ti+Fe^{3+})$ + $^{A}(Na+K)$ content varies from 1.81–2.83 apfu (Fig. 4d).

The amphibole in the two varieties of symplectite (Sec. 4.1.1) exhibits slightly variable compositions. Those forming the symplectite that partially replaced the omphacite grains along their peripheries (Amp-S1) (Fig. 2d,e) have their $^{A}(2Ca+Na+K)$ and $^{C}(Al+Fe^{3+}+2Ti)$ contents within 0.21–0.63 apfu and 0.47–1.21 apfu, respectively (Fig. 4a). The Si contents and $Mg/(Mg+Fe^{2+})$ ratios of these amphibole grains range between 6.75–7.34 apfu and 0.72–0.84 (Fig. 4b). The $^{C}(Al+Fe^{3+}+2Ti)$ contents for most of these grains are lower than those constituting the matrix (Amp-M), whereas their Si contents are higher than the latter. The ^{B}Na (0.02–0.30 apfu) and $^{C}(Al+Ti+Fe^{3+})$ + $^{A}(Na+K)$ (0.70–1.72 apfu) contents are also lower than Amp-M (Fig. 4c,d). Compositionally, the Amp-S1 grains mostly plot in the magnesiohornblende fields in the $^{C}(Al+Fe^{3+}+2Ti)$ vs. $^{A}(2Ca+Na+K)$ (Hawthorne et al. 2012) and Si vs. $Mg/(Mg+Fe^{2+})$ (Ca_A < 0.5) (Leake et al. 1997) classification diagrams. The second category of amphibole (Amp-S2) is present in the symplectite that wholly replaced the precursor omphacite. These Amp-S2 grains exhibit $^{A}(2Ca+Na+K)$ and $^{C}(Al+Fe^{3+}+2Ti)$ contents of 0.02–0.50 apfu and 0.24–1.28 apfu, respectively (Fig. 4a). The Si contents and $Mg/(Mg+Fe^{2+})$ ratios of these grains range between 7.29 –7.79 apfu and 0.74–0.85 (Fig. 4b). The Na content at the B-site and the $^{C}(Al+Ti+Fe^{3+})$ + $^{A}(Na+K)$ content for Amp-S2 vary from 0.07–0.41 apfu and 0.28–1.77 apfu, respectively (Fig. 4c,d), both of which are lower than those of Amp-M.

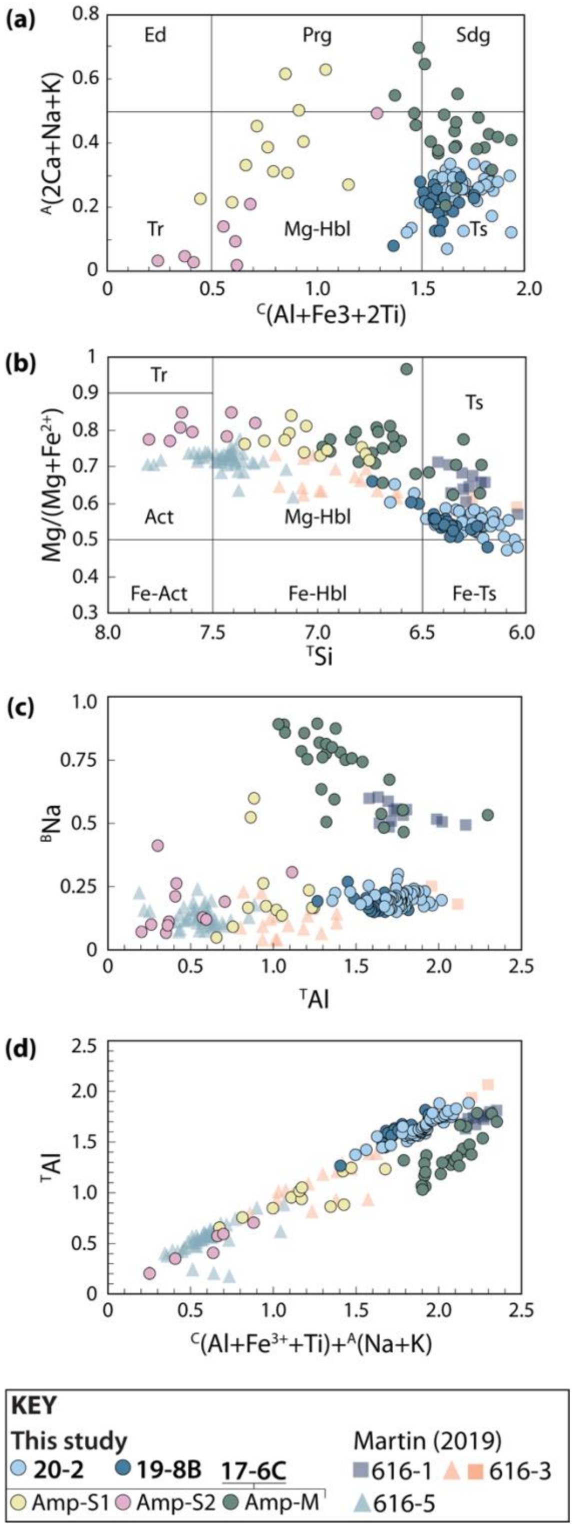

Fig. 4. *EPMA-derived amphibole mineral chemistry data from the eclogite and garnet amphibolite samples. Classification diagrams for calcic amphibole* ***(a)*** *after Hawthorne et al. (2012) and* ***(b)*** *after Leake et al. (1997). Correlation plots of* ***(c)*** *Al_{total} (^{T}Al+^{C}Al) vs. $^{B}X_{Ca}$,* ***(d)*** *$^{C}(Al+Fe^{3+}+Ti)$ + $^{A}(Na+K)$ vs. ^{T}Al (Robinson et al. 1971), and* ***(e)*** *^{T}Al v/s ^{B}Na (Brown 1977). Amp-S1 and Amp-S2 refer to the amphibole present in the two categories of symplectite, and Amp-M refers to the matrix amphibole (Sec. 4.2.1). Abbreviations-: Fe-Act: ferro-actinolite, Fe-Hbl: ferro-hornblende, Fe-Ts: ferri-tschermakite, and Mg-Hbl: magnesiohornblende. The rest*

of the mineral abbreviations are after Whitney and Evans (2010). Microprobe data of amphibole from the eclogites of the Western Gneiss Region (Norway) are also shown for easier comparison (Martin 2019). The mineral formula for this data is also recalculated based on 23 oxygens and 13 cations (excluding Ca, Na, K). The triangles and squares correspond to the amphibole of the symplectite and matrix around the garnet porphyroblasts, respectively. The degree of retrogression and amphibole content of the symplectites increases from sample 616-1 to 616-3 to 616-5.

4.2.2 Garnet amphibolites (samples 19-8B and 20-2)

The amphibole in the two garnet amphibolite samples is compositionally similar (Tables ST5 and ST6 in Supplementary File S1). However, some compositional differences exist between the amphibole of the garnet amphibolites and that of the eclogite. Firstly, these amphiboles mostly plot in the Tschermakite fields of the ^{C}(Al+Fe^{3+}+2Ti) vs. ^{A}(2Ca+Na+K) and the Si vs. Mg/(Mg+Fe^{2+}) classification diagrams of Hawthorne et al. (2012) and Leake *et al.*, (1997), respectively (Fig. 4a). The ^{A}(2Ca+Na+K) and ^{C}(Al+Fe^{3+}+2Ti) contents of the amphibole of sample 20-2 vary between 0.07–0.33 apfu and 1.42–1.93 apfu, respectively, whereas those of sample 19-8B fall within the range 0.08–0.30 apfu and 1.36–1.75 apfu, respectively. Although the ^{C}(Al+Fe^{3+}+2Ti) content is comparable to that of the amphibole of the eclogite matrix, it is much higher than that of the symplectite. The Si content of the amphibole in samples 19-8B and 20-2 is in the range of 5.98–6.65 apfu and 6.18–6.73 apfu, respectively, and are lower than most of the matrix amphibole and all the amphibole that constitute the symplectites of the eclogite (Fig. 4b). Similarly, the Mg/(Mg+Fe^{2+}) ratio of the amphibole in both samples 19-8B and 20-2 lie within 0.47–0.66 and are lower than those of the eclogite (Fig. 4b). The amphibole grains of sample 19-8B and 20-2 show similar ^{B}Na (Fig. 4c) and ^{C}(Al+Ti+Fe^{3+}) + ^{A}(Na+K) (Fig. 4d) contents that range within 0.15–0.30 apfu and 1.40–2.18 apfu, respectively. These values are lower than those of the matrix amphibole grains in the eclogite sample 17-6C.

4.3 Petrofabric analysis

4.3.1 Crystallographic preferred orientations

Site 1S from sample 17-6C comprises elliptical omphacite grains surrounded by much finer grains of amphibole (Fig. 5a, fig. SF2a in Supplementary File S1). Although the overall orientation of each omphacite is different from the others, the lack of variations in the orientations within each grain is evident in the orientation (IPF-X) map (Fig. 5b). The amphibole CPO distributions show that their <001> are concentrated at three isolated locations that are distributed along a girdle (Fig.5c). The <100> and <010> are also distributed along girdles at a low angle to one another. The girdle for the <100> is nearly parallel to the overall orientation of the long axes of the omphacite grains of the EBSD mapped area (Fig. 5c). The pole figures for this region demonstrate that the CPO distributions of the amphibole (Fig. 5c) nearly match with those of the omphacite (Fig. 5d). Such a correlation is also observed in Site 1S-A (Fig. 5e,f, fig. SF2b in Supplementary File S1).

The amphibole (Fig. 5g) and the omphacite (Fig. 5h) CPOs generated from Site 1S-A of sample 17-6C are also nearly similar. However, unlike Site 1S, the three axes of the amphibole and omphacite exhibit point maxima. Within Site 1S-A, the <001> and <010> of plagioclase (Fig. 5i) exhibit point maxima, whereas the <100> is distributed along a girdle that is nearly parallel to the plane on which the long axis of the omphacite at the centre (Fig. 5e) lies. Moreover, the <001> and <010> of plagioclase in Site 1S-A are almost parallel to the <100> and <001>, respectively, of the omphacite and amphibole and the omphacite long axes.

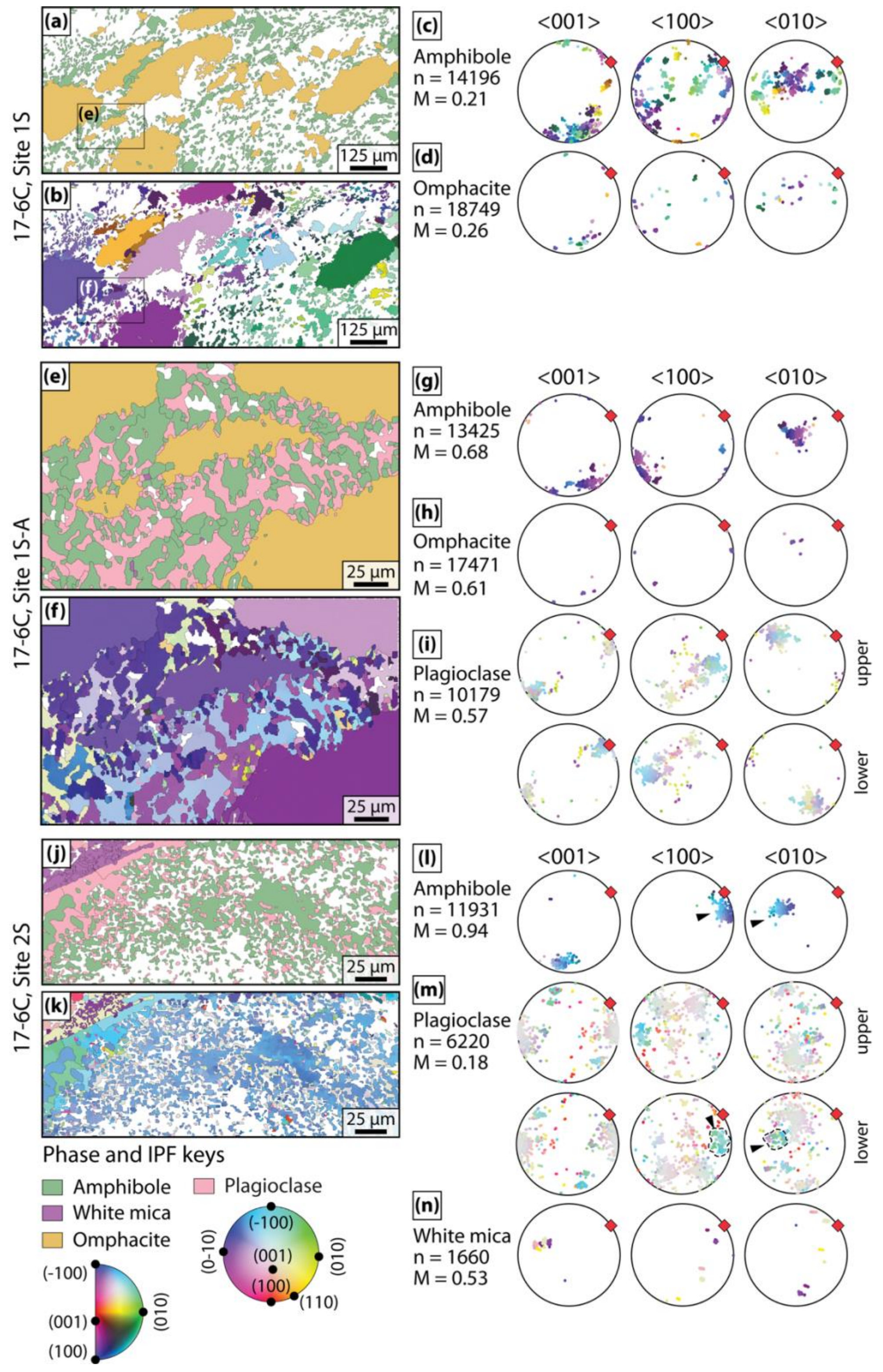

Fig. 5. *Phase maps, orientation (IPF-X) maps, and mineral CPOs from the symplectite regions of the eclogite sample 17-6C.* ***(a)****,* ***(e)****, and* ***(j)*** *are the phase maps for Site 1S, Site 1S-A, and Site 2S, respectively.* ***(b)****,* ***(f)****, and* ***(k)*** *are the orientation maps for Site 1S, Site 1S-A, and Site 2S, respectively. All orientation data points are plotted in the pole figures. Each data point in the pole figures is coded according to the orientation colour scheme (IPF key) of the corresponding mineral provided at the bottom left. The pole figures are presented as equal*

area, lower hemisphere projections (except for plagioclase, for which the upper hemisphere projections are also shown). The red diamonds at the peripheries of the pole figures mark the mean orientation of the omphacite grains. The 'bilbao' colormap of Crameri (2018) is used. n = number of orientation data points and M = misorientation index (Skemer et al. 2005).

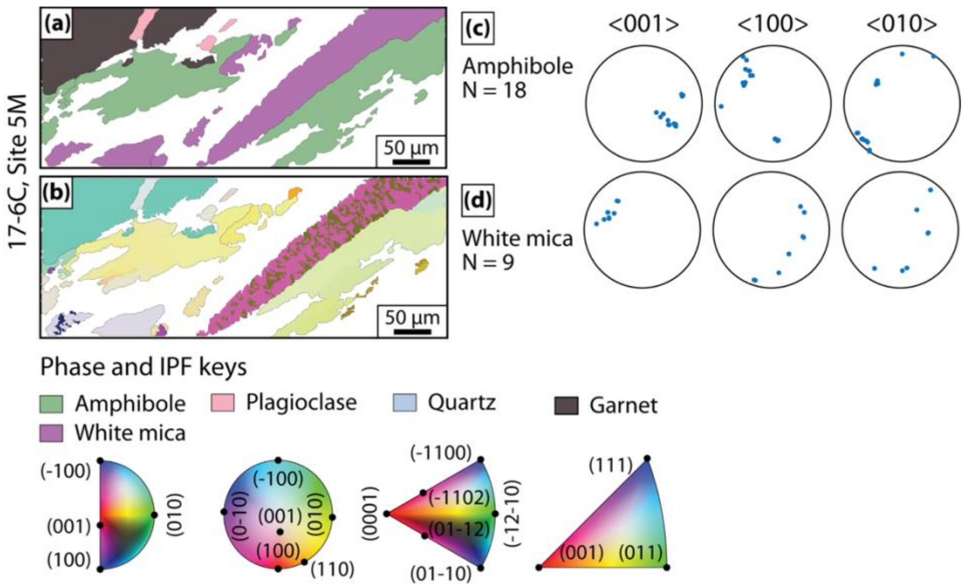

Fig. 6. *Phase maps, orientation (IPF-X) maps, and mineral CPOs from the matrix of the eclogite sample 17-6C.* ***(a)*** *phase map for Site 5M.* ***(b)*** *orientation map for Site 5M. The* ***(c)*** *amphibole and* ***(d)*** *white mica pole figures are plotted following the one-point-per-grain scheme. The pole figures are presented as equal area, lower hemisphere projections. The 'bilbao' colormap of Crameri (2018) is used. n = number of orientation data points, N = number of grains, and M = misorientation index (Skemer et al. 2005).*

The EBSD mapped symplectite of Site 2S (fig. SF2c in Supplementary File S1) lacks omphacite and mainly comprises fine-grained plagioclase in a coarse amphibole. A few white mica grains are also present (Fig. 5j,k). The three amphibole axes cluster at about the same location of the equal-area net as those of the previous Site 1S-A (Fig. 5l). Although the plagioclase <001> and <010> are mainly concentrated in two clusters and the <100> forms a weak girdle, the overall distributions in the three pole figures are relatively weaker than that of Site 1S-A (Fig. 5m). In addition to the plagioclase <001> and <010> being parallel to the <100> and <001>, respectively, of the amphibole, some of the plagioclase grains also have their <100> and <010> parallel to the those of some amphibole grains (marked with black arrowheads in Fig. 5l,m). The white mica <001> is clustered, whereas the <100> and <010> exhibit girdle distributions (Fig. 5n).

A few (<20) amphibole and white mica grains from the matrix of the eclogite sample 17-6C are also mapped for EBSD data (Fig. 6a,b). The amphibole <001> and <100> are clustered, whereas the <010> are distributed along a girdle (Fig. 6c). The <001> of the white mica is also concentrated at a point, but the <100> and <010> exhibit girdle distributions (Fig. 6d).

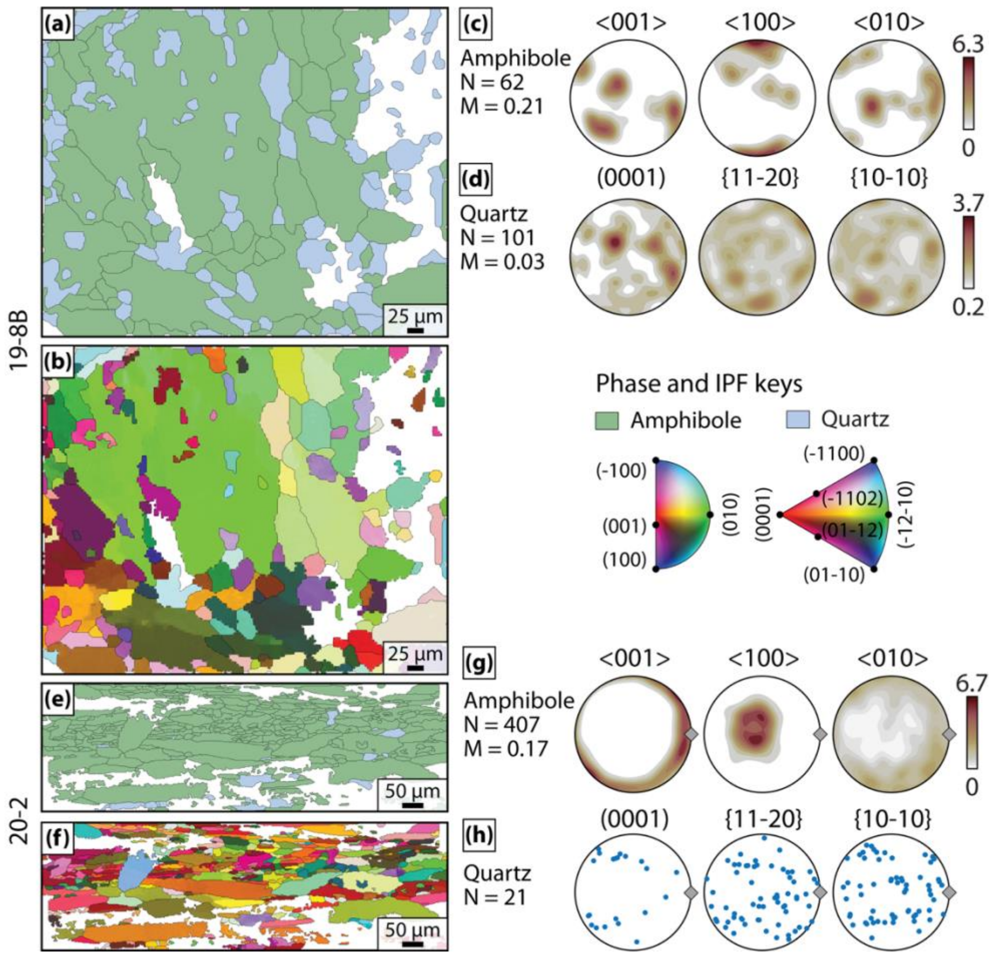

Fig. 7. *Phase maps, orientation maps, and mineral CPOs from the garnet amphibolite samples.* ***(a)*** *and* ***(e)*** *are the phase maps for samples 19-8B and 20-2, respectively.* ***(b)*** *and* ***(g)*** *are the orientation maps for samples 19-8B and 20-2, respectively. The one-point-per-grain pole figures of* ***(c,d)*** *19-8B and* ***(g,h)*** *20-2 are presented as equal area, lower hemisphere projections. They are contoured to multiples of uniform density when at least 50 grains are present. The 'bilbao' colormap of Crameri (2018) is used. The gray diamonds at the peripheries of the pole figures mark the mean orientation of the amphibole grains. N = number of grains and M = misorientation index (Skemer et al. 2005).*

The EBSD data from sample 19-8B is also obtained from a region dominated by amphibole (Fig. 7e). Intragrain variations in amphibole are more prominent than those in quartz (Fig. 7f). The amphibole in this sample shows strong CPOs (Fig. 7g). The <001> is concentrated in four isolated clusters, three of which lie on a girdle that passes through the center of the equal area net. The <100> exhibits a point maximum as well. The two clusters are formed near the periphery of the equal area net and at about 45° to the girdle formed by the <001>. The <010> is distributed along a girdle parallel to the periphery and forms a cluster near the center of the equal area net. The quartz CPOs are weak (Fig. 7h).

In sample 20-2, amphibole is dominant in the region mapped for EBSD data with much fewer quartz (Fig. 7e). Intragrain changes in orientations in the amphibole are visible in the orientation map (Fig. 7f). The CPO distributions of the amphibole (Fig. 7g) are relatively stronger than those of quartz (Fig. 7h). The <001> and <010> of the amphibole are distributed along girdles that are nearly parallel to the periphery of the equal area net, i.e., the surface of observation of the sample. The CPO of the latter is relatively weaker than the former. The <100> CPO is strongly clustered. The poles to the (0001), {11-20}, and {10-10} of quartz, on the other hand, do not exhibit any preferred orientation (Fig. 7h).

4.3.2 Misorientation analysis

The low-angle (2–<10°) and correlated high-angle (≥10°) misorientation axes, referred to as LAXs and HAXs, respectively, henceforth, of the amphibole in Site 1S-A of sample 17-6C show strong crystallographic control (Fig. 8a-c). The LAXs are mainly distributed along the (100) with maxima parallel to <001> and <010>, the latter being more prominent (Fig. 8a). The HAXs are preferentially oriented parallel to the <001> with two sub-maxima parallel to the poles of (100) and (-100) (Fig. 8b,c). The LAXs in the case of Site 2S are mainly distributed on (100) with a cluster parallel to <001>. But their overall distribution is weaker than that of Site 1S-A (Fig. 8d). The HAXs are also more randomly distributed compared to those of Site 1S-A (Fig. 8e).

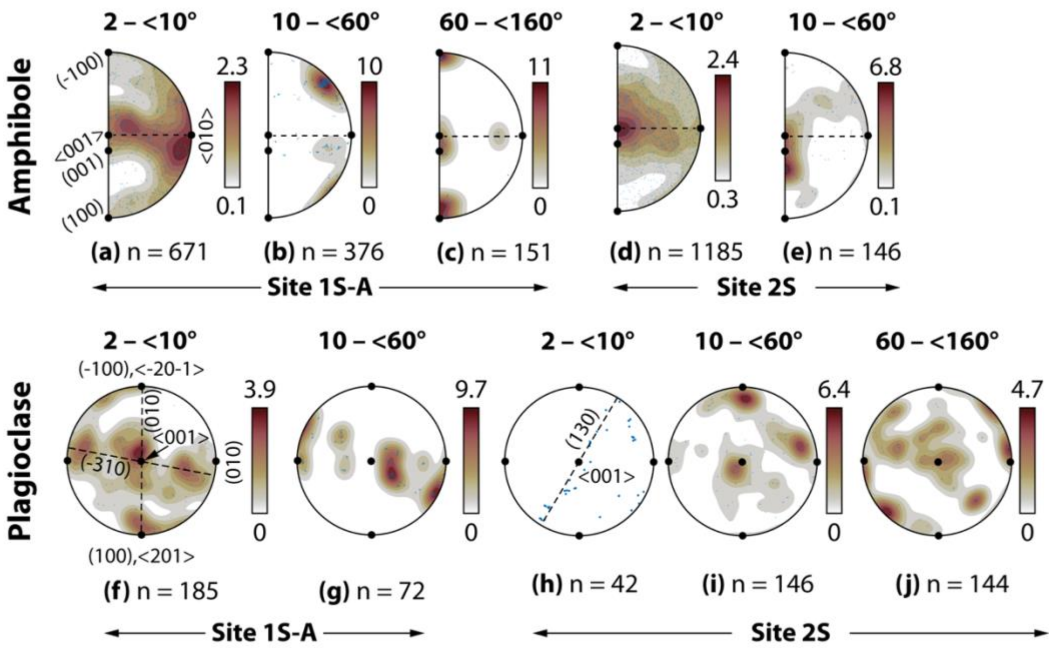

Fig. 8. *Distributions of the low-angle (LAX, 2–<10°) and correlated high-angle (HAX, ≥10–160°) misorientation axes in crystal coordinate systems. Amphibole* ***(a)*** *LAXs and* ***(b,c)*** *HAXs from the symplectite Site 1S-A. Amphibole* ***(d)*** *LAXs and* ***(e)*** *HAXs from the symplectite Site 2S. Plagioclase* ***(f)*** *LAXs and* ***(g)*** *HAXs from the symplectite Site 1S-A. Plagioclase* ***(h)*** *LAXs and* ***(I,j)*** *HAXs from the symplectite Site 2S. The blue dots represent individual axis orientations, which are contoured to multiples of uniform density represented by the colorbars. The 'bilbao' colormap of Crameri (2018) is used. n = number of misorientation axes.*

The plagioclase LAXs from Site 1S-A are present as isolated clusters in the crystal reference frame. These clusters are aligned along the (-310) and (010). The most dense cluster occurs nearly parallel to the <001> (Fig. 8f). The HAXs of these plagioclase grains are mostly either parallel to the <001> axes or perpendicular to the (010) (Fig. 8g). Plagioclase LAXs from Site 2S are much fewer in number but are distributed mainly along the (130) (Fig. 8h). The HAXs, on the other hand, exhibit more random distributions compared to those of the amphibole and plagioclase of Site 1S-A (Fig. 8i,j).

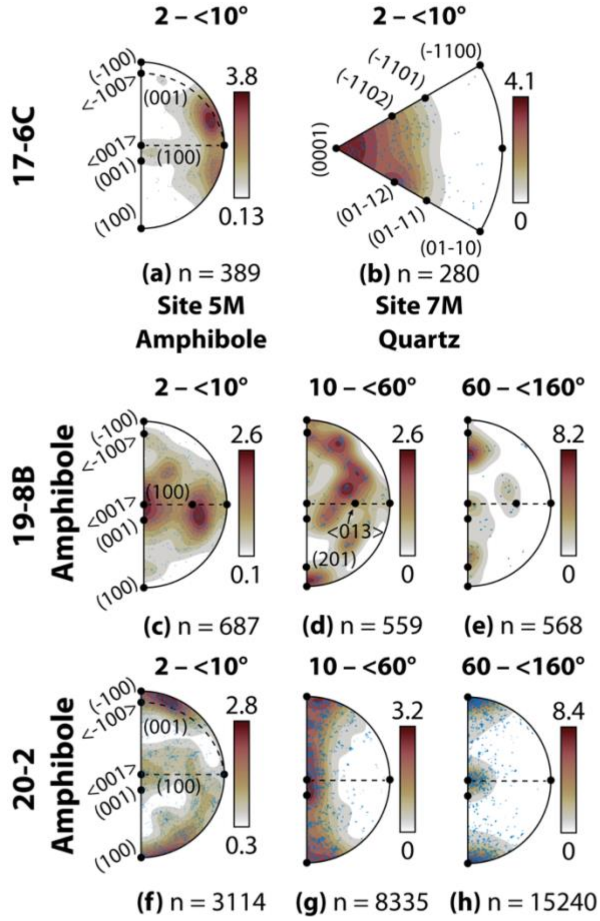

Fig. 9. *Distributions of the low-angle (LAX, 2–<10°) and correlated high-angle (HAX, ≥10–160°) misorientation axes in crystal coordinate systems. LAXs of **(a)** amphibole and **(b)** quartz grains from the eclogite matrix. **(c)** LAXs and **(d,e)** HAXs of the amphibole grains from the garnet amphibolite sample 19-8B. **(f)** LAXs and **(g,h)** HAXs of the amphibole grains from the garnet amphibolite sample 20-2. The rest of the description is the same as that of Fig. 8.*

The LAXs of amphibole and quartz from the eclogite matrix exhibit strongly preferred distributions in their respective crystal coordinate systems. Unlike the symplectite amphibole, the LAXs of matrix amphibole are parallel to the <-121>, which is nearly parallel to the pole to the (-100). Some LAXs are also parallel to the <001> (Fig. 9a). The quartz LAXs are dominantly parallel to <0001>, while the rest are parallel to the poles of the (01-12), (01-11), (-1102), and (-1101) (Fig. 9b). The distribution of the LAXs of amphibole of sample 19-8B is like that observed for the amphibole LAXs of sample 17-6C. They are mostly distributed parallel to the (100) and strong clusters parallel to the <001> axis and nearly parallel to the

<013> (Fig. 9c). The HAXs are also preferentially oriented with maxima parallel to the <-100> and two sub-maxima parallel to the <013> and to the poles of the (201) (Fig. 9d,e). In sample 20-2, the LAXs of amphibole (Fig. 9f) show strongly preferred distributions. Unlike those in sample 17-6C, they are mostly parallel to the poles of the (110) and (100), with relatively fewer being parallel to the <001>. Their HAXs are strongly clustered parallel to the <001> and perpendicular to the (100) in the crystal reference frame (Fig. 9g,h).

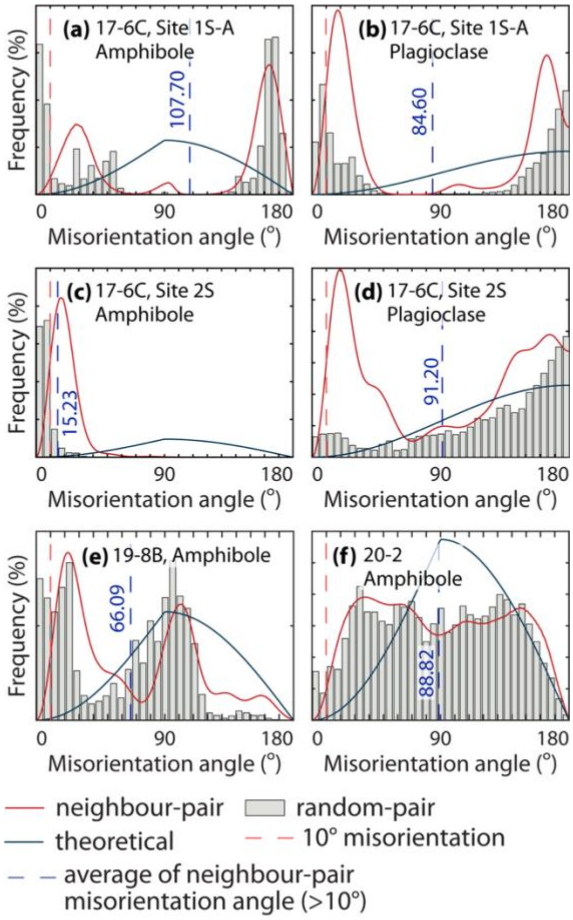

Fig. 10. *Misorientation angle distributions (MADs).* ***(a)*** *Amphibole and* ***(b)*** *plagioclase MADs from Site 1S-A of the eclogite sample 17-6C.* ***(c)*** *Amphibole and* ***(d)*** *plagioclase MADs from Site 2S of sample 17-6C. MADs of amphibole grains from the garnet amphibolite samples* ***(e)*** *19-8B and* ***(f)*** *20-2. The vertical bars represent the frequency distribution of the random-pair misorientations. The neighbour-pair and theoretical misorientation angle distributions are represented by the red and dark green frequency curves.*

The misorientation angle distributions (MADs) for neighbour-pair and random-pair of grains are determined. Since the frequencies of low-angle (2–<10°) boundaries are higher than those of the rest of the bins, the neighbour-pair MADs corresponding to misorientations of 10° or higher are shown only. Within Site 1S-A, both the neighbour-pair and random-pair MADs of amphibole (Fig. 10a) and plagioclase (Fig. 10b) are discontinuous and particularly characterized by the scarce or complete lack of neighbour- and random-pairs of grains with misorientations ranging between 55–135°. The frequencies of the neighbour-pair and random-pair MADs of amphibole and plagioclase are higher than their theoretical distributions for misorientations <50° and >160°. The neighbour-pair and random-pair MADs of amphibole in Site 2S are mainly restricted to lower angles (<20°), where both the MADs show higher frequencies than the theoretical distribution (Fig. 10c). Adjacent amphibole with higher misorientations are scarce and discontinuous. The neighbour-pair MAD of plagioclase shows higher frequencies than the random-pair and theoretical distributions for <50° misorientations. The frequencies drop between 50–160°, lower than the theoretical distribution, but follow the random-pair distribution. The neighbour-pair MAD is higher than the rest of the two again at >160° misorientations (Fig. 10d). The frequencies of the random-pair MAD increase gradually with the misorientation angles. Still, they remain lower than those of the theoretical distribution within 55–155° (Fig. 10d).

In sample 19-8B, the random- and neighbour-pair MADs of amphibole are nearly similar. However, the former is lower than the latter in the angular ranges 15–60° and >115°. The frequencies of both distributions are higher than the theoretical distribution at <40° and 95–105° (Fig. 10e). The neighbour-pair and random-pair MADs of amphibole in the garnet amphibolite sample 20-2 show distinct deviation from the theoretical and are characterised by a plateau at intermediate misorientation (35–150°). The neighbour-pair and random-pair MADs closely follow each other throughout and exhibit lower frequencies than those of the theoretical distribution only within 65–145°. (Fig. 10f).

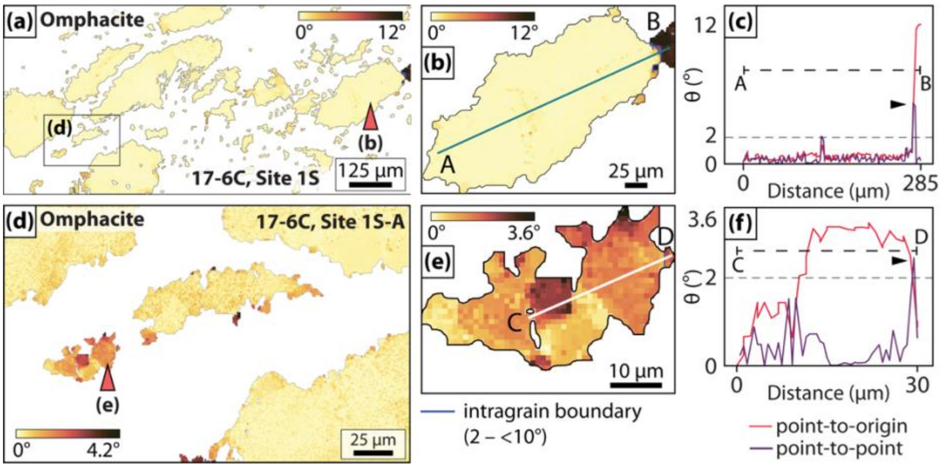

__Fig. 11.__ Misorientation (θ) to grain mean orientation (mis2mean) maps and misorientation profiles from the eclogite sample 17-6C. __(a)__ mis2mean map of omphacite from Site 1S. __(b)__ mis2mean map and __(c)__ misorientation profile of one of the omphacite grains (red arrowhead in __(a)__). __(d)__ mis2mean map of the omphacite from Site 1S-A. __(e)__ mis2mean map and __(f)__ misorientation profile of one of the grains (red arrowhead in __(d)__). The black arrowheads in the misorientation profiles point to the misorientation angle peaks corresponding to the subgrain boundaries. The 'lajolla' colormap of Crameri (2018) is used for all the mis2mean maps. Each colour bar represents the angular range of misorientation of the corresponding map/grain.

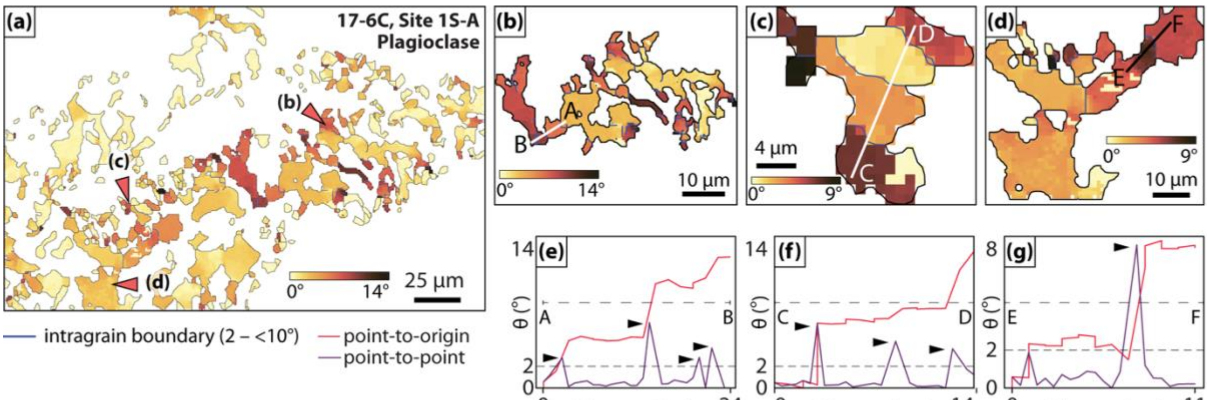

__Fig. 12.__ Misorientation (θ) to grain mean orientation (mis2mean) maps and misorientation profiles of selected plagioclase grains from the eclogite sample 17-6C. __(a)__ mis2mean map of plagioclase in the symplectite from Site 1S-A. __(b-d)__ mis2mean maps of selected plagioclase grains (red arrowhead in __(a)__). Misorientation profiles along __(e)__ A-B, __(f)__ C-D, and __(E-F)__ line segments in the plagioclase grains of __(b)__, __(c)__, and __(d)__, respectively. The rest of the description is the same as that of Fig. 11.

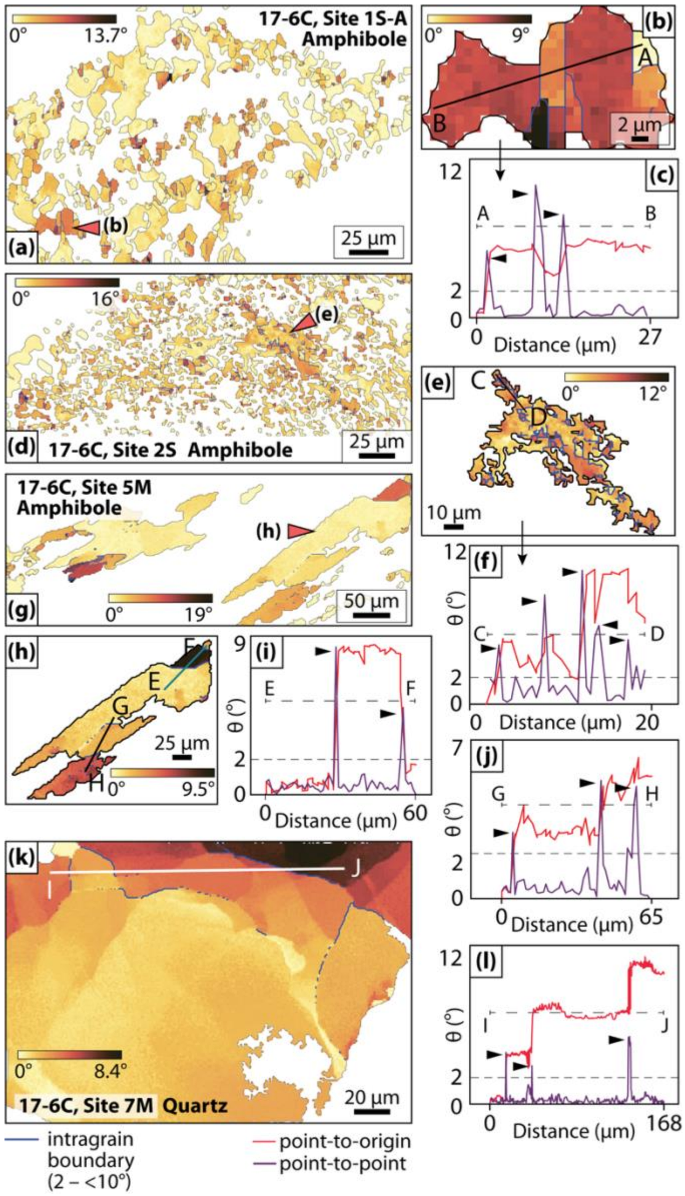

Fig. 13. *Misorientation (θ) to grain mean orientation (mis2mean) maps and misorientation profiles of selected grains from the eclogite sample 17-6C. mis2mean map of **(a)** all amphibole grains and **(b)** one selected amphibole grain (red arrowhead in **(a)**) from the symplectite in Site 1S-A. **(c)** Misorientation profile along the A-B line segment in **(b)**. **(d)** mis2mean map of amphibole in the symplectite from Site 2S. **(e)** mis2mean map of a selected amphibole grain (red arrowhead in **(d)**). The misorientation profile along the line segments C-D is illustrated in **(f)**. **(g)** mis2mean map of amphibole from the matrix (Site 5M). **(h)** mis2mean map of a selected amphibole grain (red arrowhead in **(g)**). The misorientation profiles along the line segments E-F and G-H are illustrated in **(i)** and **(j)**, respectively. **(k)** mis2mean map of a quartz grain from the matrix (Site 7M). **(i)** illustrates the misorientation profiles along the line segment I-J. The rest of the description is the same as that of Fig. 11.*

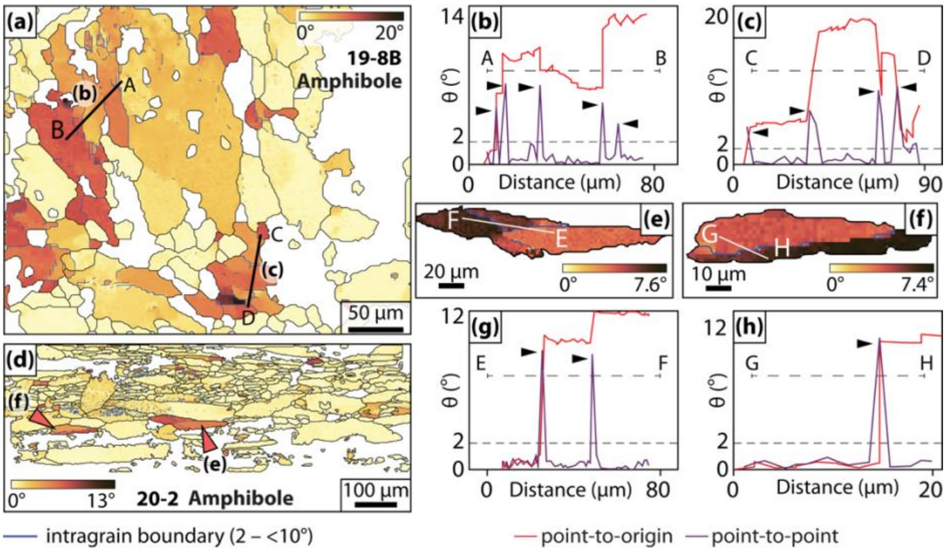

Fig. 14. *Misorientation (θ) to grain mean orientation (mis2mean) maps and misorientation profiles of selected grains from the garnet amphibolites.* ***(a)*** *mis2mean map of amphibole from the sample 19-8B.* ***(b)*** *and* ***(c)*** *are the misorientation profiles along the line segments A–B and C–D, respectively, marked in* ***(a)****. The mis2mean map of* ***(d)*** *all the amphibole grains and* ***(e,f)*** *two selected amphibole grains (red arrowheads in* ***(d)****) from the sample 20-2.* ***(g)*** *and* ***(h)*** *illustrate the misorientation profiles along the line segments* ***(e)*** *E–F and* ***(f)*** *G–H, respectively. The rest of the description is the same as that of Fig. 11.*

Maps depicting the intragranular misorientations between each pixel and the mis2mean and misorientation line profiles within selected grains with visible subgrain boundaries show that subgrains are scarce in omphacite and much more prominent in the rest of the minerals. The omphacite from Site 1S (Fig. 11a) of sample 17-6C shows a maximum mis2mean value of 12° (Fig. 11b). The misorientation angle across the subgrain boundary is nearly 4° (Fig. 11c). Another finer omphacite grain from Site 1S-A (Fig. 11d) has a maximum mis2mean value of 3.6° (Fig. 11e) and misorientation variation across the only subgrain boundary is slightly above 2° (Fig. 11f). Some of the plagioclase grains present in the symplectite of Site 1S-A (Fig. 12a) show relatively higher maxima of mis2mean values of 14° (Fig. 12b), 9° (Fig. 12c), and 9° (Fig. 12d) with the misorientations across some of the subgrain boundaries being >6° (Fig. 12e,f,g). The amphiboles from the same symplectite region (Site 1S-A) also show a mis2mean maximum of 13.7° (Fig. 13a). One of these grains with well-developed subgrain boundaries shows a maximum mis2mean value of 9° (Fig. 13b) with the misorientation angle across the subgrain boundaries ranging between 5° to ~10° (Fig. 13c).

Subgrains are also present in some amphiboles in the matrix of the eclogite sample 17-6C (Fig. 13g). The maximum mis2mean value in one of these grains is 9.5° (Fig. 13h), and the change in the misorientation angles across some of its subgrain boundaries are nearly 8° (Fig. 13i) and 5° (Fig. 13j). One of the quartz grains in the eclogite matrix consists of subgrain boundaries much longer than those preserved in the amphibole grains (Fig. 13k). The misorientations across these boundaries range within 3–6° (Fig. 13l). The amphibole in sample 19-8B also contain subgrains (Fig. 14a). The misorientations across these range within 3–8° (Fig. 14b,h). Subgrain boundaries are also present in some of the amphiboles in sample 20-2 (Fig. 14d–f), with the misorientations across some of them being >8° (Fig. 14g,h).

5. Discussions

5.1 Deformation characteristics of the symplectite and matrix constituents in the eclogite

5.1.1 *Omphacite*

Omphacite occurs as clusters of elliptical grains. Although the omphacites within a cluster exhibit a clear shape preferred orientation, which reportedly developed at ~580 °C (de Sigoyer et al. 2004), they do not appear to be strongly deformed by dislocation creep, because of which the intragranular misorientation variation is gentle and subgrain boundaries are scarce and poorly developed (Fig. 11). Omphacite can deform via dislocation creep and produce subgrains at temperatures as low as ~470 °C (Piepenbreier and Stöckhert 2001). Previous thermobarometric (e.g., de Sigoyer et al., 1997; St-Onge et al., 2013) and EBSD-based CPO studies (Dutta and Mukherjee 2021; Dey et al. 2022) have shown that the eclogite and the enclosing granite gneiss of the Tso Morari region have experienced temperatures >600 °C. Given the insignificant dynamic recrystallization of the omphacite in the eclogite sample 17-6C, post-deformation annealing at an elevated temperature, such as the predicted thermal peak for the Tso Morari eclogite at mid-crustal depths (7–12 kbar) during exhumation (Guillot et al. 1997; de Sigoyer et al. 1997; St-Onge et al. 2013; Wilke et al. 2015), could be responsible for limited subgrain development (Brenker et al. 2002).

Despite restricted subgrain development, omphacite exhibits clustered CPO distributions (Figs 5d,h). Therefore, we infer that the omphacite CPOs have resulted from their anisotropic growth, which has previously been observed in eclogites (Godard and Van Roermund 1995; Mauler et al. 2001; Stöckhert 2002; Rogowitz and Huet 2021). In most cases, the anisotropic shapes of omphacite crystals are attributed to their oriented growth, which also produces the strong CPOs. Diffusive mass transfer processes such as dissolution-precipitation, diffusion creep, and pressure solution can further accentuate the shape (Mauler et al. 2001; Cao et al. 2011; McNamara et al. 2024), and result in asymmetric zoned omphacite crystals (Stünitz et al. 2020; McNamara et al. 2024). The lack of chemically zoned omphacite grains in the studied eclogite 17-6C (fig. SF5 in Supplementary File S1) suggests that volume diffusion or Nabarro-Herring creep produced the anisotropic crystals.

Unlike the scarcity of plastic deformation signatures, brittle fractures are more prominent in the omphacite grains. Most of these transgranular fractures have developed parallel to the short axis of the grains (Fig. 2c,d,g). These fractures originated as Mode-I or extensional fractures because they do not exhibit shear displacement parallel to their walls (Paterson and Wong 2005). Although tectonic forces can produce brittle fracture, it is common for them to originate in metamorphic rocks due to fluid overpressure (Pennacchioni 1996; Wawrzenitz et al. 2019) or reaction-induced volume change (Jamtveit et al. 2009) or both (Engvik et al. 2001). Limited permeability coupled with continued fluid ingress can result in stress perturbations at the grain boundaries and, consequently, fracturing of the grains (Cox and Etheridge 1989; Pennacchioni 1996; Brander et al. 2012; Kelemen and Hirth 2012). Hydration reaction or mineral transformation characterised by volume increase or density lowering can also generate stresses high enough to facilitate grain-scale fracturing. For example, Engvik et al. (2001) reported fractured garnet due to grain-scale volume increase caused by localised hydration of olivine, diopside, and orthopyroxene to amphibole and talc in the gabbro from the UHP Western Gneiss Region (Norway). Replacement of rutile by titanite and subsequent fracturing of the former due to the positive dilatancy of the reaction is another such example (Wawrzenitz et al. 2019). The amphibole-plagioclase (± diopside) symplectite after omphacite in the studied eclogite was produced by Omphacite + SiO_2 → Diopside + Na-Plagioclase + H_2O → (Na,Ca)-Amphibole + Na-Plagioclase (± Diopside). The products diopside (density = 3.2 g cm^{-3}), Na-plagioclase (2.6 g cm^{-3}), and Na-Ca-Amphibole (3.1 g cm^{-3}) are less dense than the reactant Omphacite (3.4 g cm^{-3}) (Deer et al. 2013) and thus will occupy larger volumes than their parent. Therefore, we propose that the fractures in the omphacite grains originated at their peripheries in response to the stress perturbations resulting from the combined effect of localised fluid overpressures because of restricted permeability and volume increase associated with the symplectitisation. We observed that the traces of (100), the common cleavage of omphacite (Deer et al. 2013), are parallel to the shorter axes of some of the omphacite grains in the EBSD mapped regions (fig. SF6 in Supplementary File S1). They acted as weak planes and dictated the orientation of the transgranular fractures, which were subsequently invaded by hydrous fluids producing the narrow bands of symplectitised zones (Fig. 2c,d,i).

5.1.2 Plagioclase and Amphibole

The plagioclase investigated in this study belongs to the symplectite complexes produced due to the breakdown of the omphacites, and they, along with amphibole in the symplectite complexes, mainly display clustered point distributions (Fig. 5c,g,i,l,m). In the case of amphibole, these point clusters are occasionally distributed over girdles (Figs 5c). Overall, their CPO distributions demonstrate crystallographic inheritance from the parent omphacite, which is typical for the product phases of breakdown reactions forming symplectite (McNamara et al. 2012; Heidelbach and Terry 2013; Rehman et al. 2016; Cao et al. 2020; Zertani et al. 2024; Chatterjee et al. 2024). For instance, in the studied eclogite sample 17-6C, the following crystallographic relationships are observed between the product amphibole and plagioclase grains and their parent omphacite crystals: $<001>_{Amp}//<001>_{Omp}$, $<010>_{Amp}//<010>_{Omp}$, and $<100>_{Amp}//<100>_{Omp}$ (Fig. 5c,d,g,h). These parallelisms are particularly demonstrated in the symplectites from Sites 1S and 1S-A, with the latter resembling the symplectite category S1 (Fig. 5c,d,g,h). Similar crystallographic relationships ($<010>_{Plag}//<001>_{Omp}$ and $<001>_{Plag}//<100>_{Omp}$) are also demonstrated between plagioclase and omphacite in Site 1S-A (Fig. 5h,i). Furthermore, the <100> and <001> of amphibole and plagioclase, respectively, belonging to the symplectite, are oriented parallel to the long axes of their parent omphacite (Fig. 5c,d,g–i). The symplectite of Site 2S, where the parent omphacite is completely consumed by the amphibole-plagioclase symplectite (category S2), also preserves the expected crystallographic relationships between amphibole and plagioclase, such as $<001>_{Amp}//<010>_{Plag}$ and $<100>_{Amp}//<001>_{Plag}$ (Fig. 5l,m). The orientations of the amphibole <100> and plagioclase <001>, in this case, probably indicate the long axis direction of the parent omphacite.

The high degree of misfits between the theoretical and random-pair MADs of the amphiboles and plagioclases in the mapped symplectite regions are a consequence of the non-random CPO distributions (Fig. 10a–d), which have also caused the greater frequencies of the neighbour-pair MADs than both the random-pair and theoretical MADs at lower angles (<60°). Such high frequencies of neighbour-pair MADs could also result from subgrain rotation recrystallization (Svahnberg and Piazolo 2010), but the crystallographic relationships between the parent omphacite, amphibole, and plagioclase discussed above suggest that inheritance during replacement is more likely to have resulted in such correlated neighbour-pair MADs (Wheeler et al. 2001).

The LAX distributions of plagioclase present in Site 1S-A, assuming tilt geometries for the subgrain boundaries, are roughly consistent with <201>(010), with minor contributions from <001>(010) and <001>(-310) slip systems (Fig. 8f). Of these, <001>(010) and <201>(010) have been previously reported as slip directions for plagioclase, which deformed naturally by dislocation creep (Olsen and Kohlstedt 1984; Ji and Mainprice 1990;

Kruse et al. 2001; Svahnberg and Piazolo 2010; Allard et al. 2021). The LAXs of amphibole in the mapped symplectite of Site 1S-A are preferentially distributed parallel to the (100) with clusters parallel to the <010> (Fig. 8a), suggesting that intracrystalline deformation was dominantly accommodated by the <001>(100) slip system if we assume a tilt subgrain boundary (Lloyd et al. 1997). Although the amphibole and plagioclase LAXs from Site 2S are preferentially distributed along the (100) and (130), respectively, the HAXs between the pairs of adjacent amphibole (Fig. 8e) and plagioclase (Fig. 8i,j) are also more randomly distributed in the crystal reference frames compared to those of Site 1S-A (Fig. 8a,f). One of the possibilities for such distribution could be that the symplectite constituents of Site 2S, unlike those of Site 1S-A, were deformed in the presence of hydrous fluid by grain boundary sliding (Jiang et al. 2000; Svahnberg and Piazolo 2010; Fukuda and Okudaira 2013).

<001>(100) is the primary slip system for amphibole deformed via dislocation creep and has been widely reported in experimentally (Dollinger and Blacic 1975; Rooney et al. 1975; Morrison-Smith 1976; Ko and Jung 2015) as well as naturally deformed rocks (Skrotzki 1992; Berger and Stünitz 1996; Díaz Aspiroz et al. 2007; Cao et al. 2010; Elyaszadeh et al. 2018). Since the slip direction and misorientation axis should be perpendicular for a tilt boundary, dominance of <001>(100) cannot explain the cluster of intragrain misorientation axes parallel to the <001>. Such discordance, in the absence of evidence of microfracture or rigid body rotation in the symplectite amphibole, possibly suggests that the subgrain boundaries are composed of both tilt and twist characteristics, and each LAX in the observed cluster parallel to the <001> resulted as the average of multiple misorientation axes associated with different slip systems (Lloyd 2004; Díaz Aspiroz et al. 2007). Crystal distortion and subgrain boundary development are also observed in the amphibole of the eclogite matrix (Fig. 12g–j). The LAXs for these amphiboles cluster on the (001) and at low-angles to the <010>, implying glide of dislocations on either <-100>(001) or <001>(100) systems (Fig. 8f). Slip on the (001), however, would require the amphibole I-beam chains to break (Hacker and Christie 1990), and is reported only from single hornblende crystals deformed experimentally at

≤600°C (Morrison-Smith 1976). Therefore, <001>(100) is more likely to be the active slip system.

Microstructural observations in naturally and experimentally produced symplectites indicate that either diffusion creep (Zertani et al. 2024) or dislocation creep (Odashima et al. 2007; Zhao et al. 2012) or sequential operation of these mechanisms (Doi et al. 2014) can facilitate their post-nucleation deformation. Symplectite with constituent grains lacking evident intracrystalline plastic deformation is also reported (e.g., Heidelbach and Terry, 2013). Although the point-maxima CPO distributions of amphibole and plagioclase of the symplectites examined in this study are majorly inherited from the parent omphacites, the contributions of dislocation-mediated deformation of the amphibole and plagioclase cannot be discarded entirely. The strong crystallographic control on the LAX distributions of amphibole (Fig. 8a,d) and plagioclase (Fig. 8f) and the evident subgrain boundary development (Figs 11, 12a–f) supports the possibility of their deformation via dislocation creep (Díaz Aspiroz et al. 2007; Keppler et al. 2016; Van Der Werf et al. 2017; Liu and Cao 2023). Continuous lattice bending of at least some of the plagioclase (Fig. 12) and amphibole (Fig. 13a–c) grains present within Site 1S-A is also evident in the mis2mean maps. Moreover, lack of subgrains in the parent omphacite grains (Fig. 10) precludes the possibility of inheritance of deformed lattice and subgrain walls (Bestmann et al. 2005; Svahnberg and Piazolo 2010; McNamara et al. 2012; Spruzeniece et al. 2017b). Boundaries shared by slightly misoriented (<10°) adjacent grains crystallising from a common parent can be recognised as intragrain boundaries, which are typically inferred as products of plastic distortion in EBSD-derived orientation maps (Pearce et al. 2013). However, it is unlikely that the low-angle misorientation axes in such cases will exhibit non-random distributions in the crystal coordinate system.

Because of the largely continuous subgrain boundaries in the amphibole grains, we infer that 450°C marks the lower limit at which the grains deformed plastically (Biermann and Van Roermund 1983; Reynard et al. 1989; Elyaszadeh et al. 2018). The amphibole in the symplectite complexes precipitated as direct replacements of the omphacite and diopside of the diopside-plagioclase symplectite in the presence of hydrous fluids. Because plagioclase crystallised before the invasion of fluids and amphibole crystallisation, it is likely that its deformation began under dry conditions and, perhaps, continued in the presence of hydrous fluid as the amphiboles started to precipitate. However, the evidence at hand does not allow us to distinguish between the two. Dry plagioclase grains generally deform by brittle fracturing at low metamorphic grade conditions (<580 °C), whereas dislocation creep dominates at temperatures >600 °C (Olsen and Kohlstedt 1985; Kruse and Stünitz 1999; Altenberger and Wilhelm 2000; Kruse et al. 2001; Baratoux et al. 2005).

Deformation experiments have demonstrated that wet anorthites and albites are weaker (Fukuda et al. 2022; Baïsset et al. 2024) and deform in the dislocation creep regime at temperatures at least ~150 °C lower than that of the dry aggregates (Tullis and Yund 1980; Rybacki and Dresen 2000, 2004). Dislocation creep activity has also been observed at <500 °C in naturally deformed plagioclase (Shigematsu and Tanaka 2000). Therefore, plastic deformation and development of subgrain boundaries in the plagioclase grains (Fig. 11) were active even when the eclogite had exhumed to depths corresponding to <10 kbar pressure. The Na occupancies at the B-sites (Fig. 4c) further tell us that the amphibole in the symplectites formed at lower pressures than that of the matrix (Brown 1977; Palin et al. 2014).

5.1.3 *Quartz*

Quartz, one of the constituents of the eclogite matrix, consists of prominent subgrain boundaries (Fig. 2e,f) with misorientations between ~3° and 6° (Fig. 13 k,l). Such well-developed subgrain boundaries indicate that quartz accommodated deformation via the dislocation creep (e.g., Hirth and Tullis, 1992; Vernon, 2018). Assuming tilt subgrain boundaries, the clustering of the LAXs parallel to the <0001> implies the dominance of {m}<a> slip system (Lloyd et al. 1997). Additional slip systems such as the {z}<a> and {r}<a> were also active because several other LAXs are parallel to the poles of the (01-12) and (-1102), respectively (Fig. 9b). These microstructural observations suggest deformation of the matrix quartz in the temperature range of 400 to <600 °C (Baëta and Ashbee 1969; Wilson 1975; Schmid and Casey 1986; Stipp et al. 2002). Dey et al. (2022) have also reported {m}<a> slip system as the most common one from the quartz present in the matrix of retrograded and symplectite-bearing eclogites of the TMC from near the Kyagar Tso lake. Moreover, the EBSD-based c-axis study performed by Dutta and Mukherjee (2021) on the relict quartz grains present in the samples of granite gneiss, which surrounds the Tso Morari eclogites, also indicate dominance of the {m}<a>, {r}<a>, and {z}<a> slip systems. Quartz c-axis opening angle thermometry results reported by Long et al. (2020) from the granite gneiss also suggests a maximum deformation temperature of ~535 °C at pressures of 10 kbar (~35 km) or lower. These temperature estimates also match those predicted for the late-stage retrogression of the eclogite and metasedimentary rocks of the region in the amphibolite-greenschist facies conditions at <11 kbar (Guillot et al. 1997; Mukherjee et al. 2003).

5.2 Symplectite origin and evolution

Diopside-plagioclase symplectite (± amphibole ± quartz) is most commonly observed in the retrograded (U)HP eclogites (Joanny et al. 1991; Will and Schmädicke 2001; Štípská and Powell 2005; Groppo et al. 2007; Palmeri et al. 2009; Lanari et al. 2013; Renedo et al. 2015; Imayama et al. 2017; Dey et al. 2023; Zertani et al. 2024), whereas there are fewer reports of symplectite with amphibole modal amounts greater than that of the coexisting diopsidic clinopyroxene (Zhang et al. 2008; Scott et al. 2013; Liu et al. 2013; Martin 2019). The symplectite complexes of the studied eclogite sample 17/6C are almost entirely composed of amphibole and plagioclase (Fig. 5e,j). Ca-clinopyroxene grains are either much fewer than those of amphibole (Fig. 4b; Supplementary File S2) or non-existent.

Symplectite, regardless of the composition and hydroxyl ion content of the intergrown phases, requires aqueous fluid to form (Martin and Duchêne 2015; Spruzeniece et al. 2017a). Previous studies on eclogites containing amphibole-plagioclase symplectite also agree that infiltration of water or water-rich fluid produced the amphibole that either replaced the

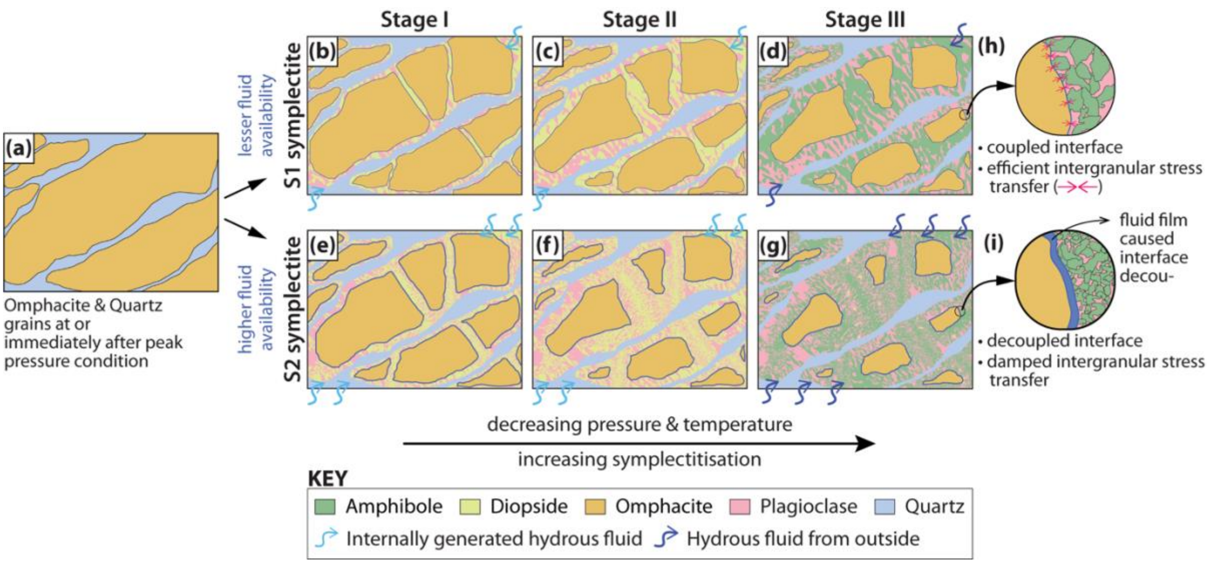

Fig. 15. *Schematic figure illustrating the sequential development of the two categories of symplectite in the studied eclogite.* ***(a)*** *Omphacite and quartz assemblage in the eclogite at or immediately after peak pressure. Progressive symplectitisation and development of* ***(b-d)*** *S1 and* ***(e-g)*** *S2 symplectites. Greater supply of hydrous fluids generated more amphibole grains in the latter case. The relatively thinner peripheries of the omphacite grains in* ***(b-d)*** *than in* ***(e-g)*** *also represent the availability of more hydrous fluids in the latter.* ***(h)*** *and* ***(i)*** *show magnified illustrations of the omphacite-symplectite interfaces for the S1 and S2 symplectites, respectively. An additional Stage IV can be visualized for the S1 and S2 symplectites as reduced size and disappearance, respectively, of the omphacite grains.*

omphacite (Liu et al. 2013; Tichomirowa and Köhler 2013) or the older diopsidic clinopyroxene in the symplectite at amphibolite facies conditions (Di Vincenzo and Palmeri 2001; Martin 2019). Although these studies did not characterise the source of the fluids, Martin (2019) argued that complete retrogression of omphacite into symplectite can only be achieved by an influx of external fluids. The author added that the breakdown of peak-pressure hydrous minerals, such as phengite, can also release fluids rich in hydrous components during decompression, and these fluids can produce amphibole crystals within the symplectite. However, because of the limited supply of such internally originated fluids, the replacement of omphacites by amphibole-bearing symplectites will be partial only. Numerous relict omphacite grains, only partially replaced by the amphibole-plagioclase symplectite (S1) at their peripheries, persist in the studied sample 17/6C (Fig. 2c,d). However, several isolated regions exist where the precursor omphacite grains are wholly transformed into amphibole-plagioclase symplectite (S2) (Fig. 2j,k). Such occurrences imply that fluid influx alone could not have driven the retrogression to completion. Its rate and extent should also have depended on the ease with which the fluid could permeate through eclogite (Straume and Austrheim 1999; Konrad-Schmolke et al. 2011; Mindaleva et al. 2020). Therefore, although hydrous fluid must have infiltrated the Tso Morari eclogite, its limited permeability restricted complete symplectitisation of the omphacite to only a few isolated pockets.

Grain boundary and microfracture can act as pathways and facilitate pervasive fluid permeation (Carter et al. 1990; Ferry 1994; Pennacchioni 1996; Jamtveit et al. 2008; Jonas et al. 2014; Mindaleva et al. 2020; Wirth et al. 2022) – a common occurrence at subduction interfaces (Lianxing et al. 2002; Konrad-Schmolke et al. 2011; Angiboust et al. 2014). O'Brien (1993) studied the retrogressed eclogites of the Münchberg Massif in Germany and reported the presence of clinopyroxene (*'less Na-rich'*) + plagioclase symplectitic corona aound the matrix quartz grains but none around the quartz inclusions within the omphacites - except for the ones connected to the matrix via fractures. Such texture exemplifies the role of grain boundary fluid in symplectitisation during exhumation and fracture in enabling fluid migration. Moreover, microfracturing can also enhance the rate and severity of retrogression, as demonstrated by the retrogressed and symplectite-bearing eclogites of Furøya Island of the Western Gneiss Region in Norway (Straume and Austrheim 1999). Thus, it could be possible that greater fluid availability in isolated pockets and the relative ease of fracturing of the precursor omphacite grains in the vicinity of those pockets acted together to produce completely symplectitised regions (S2 symplectite) in sample 17/6C (Fig. 2j,k), which is also illustrated sequentially in Fig. 15a–g. Pennacchioni (1996) showed that infiltrated fluids can cause porphyroblasts of the stronger phases, such as garnet and clinopyroxene, to fracture. The author proposed that the absence of connected fluid pathways in the metabasites from the Mt Emilium Klippe (Italy) elevated the fluid pressure locally, promoted hydrofracturing of the garnet and clinopyroxene porphyroblasts, which in turn increased the reaction surface area and facilitated their subsequent replacement by hydrous phases. He further observed that the retrograde replacement reactions remained confined to the boundaries of porphyroblasts devoid of fractures, a feature also abundant in the eclogite sample we studied (Fig. 2c,d), which further confirms that production of the amphibole-plagioclase symplectite in sample 17/6C must have progressed via dissolution-precipitation by the invading fluid (Putnis and Austrheim 2010; Spruzeniece et al. 2017a).

The EPMA data of this study demonstrate that the amphiboles constituting the S1 symplectite, Amph-S1, are relatively poorer in Si (6.78–7.24 apfu) than those present in S2 (Amph-S2, Si = 7.29–7.79 apfu) symplectite (Fig. 4b). The Amph-S2 (^{T}Al = 0.2-0.7 apfu) also plot closer to the origin along the 1:1 line in the $^{C}(Al+Ti+Fe^{3+})$ + $^{A}(Na+K)$ v/s ^{T}Al correlation diagram than Amph-S1 (^{T}Al = 0.75–1.21 apfu) (Fig. 4d), further attesting to the sequential crystallisation of Amph-S2 after Amph-S1, with progressive retrogression and symplectitisation. The amphibole EPMA data from the matrix and symplectite of the UHP eclogite of the Western Gneiss Region (Martin, 2019) match closely with those of our sample, with the Al occupancies at the tetrahedral sites of amphibole from the most retrogressed sample being the least (Fig. 4d,e).

The amphibole grains constituting the S1 symplectite have slight textural dissimilarities. Most of them are coarse and angular, whereas those closer to the omphacite boundaries are relatively finer and less angular in shape (fig. SF1c in Supplementary File S1). In the case of S2 symplectite, the finer amphibole grains are surrounded by the coarser ones (Fig. 2j,k). These textures suggest that omphacite replacement and symplectitisation progressed concentrically towards the cores of the grains such that the amphibole at the outermost rims crystallized at relatively higher temperatures, resulting in fewer nucleation sites with faster diffusion of ions and consequently coarser grains. As retrogression progressed, sluggish diffusion at relatively lower temperatures produced numerous finer-grained amphibole instead (Boland and Van Roermund 1983; Joanny et al. 1991; Lanari et al. 2013). Such a fluid-assisted concentric migration of sharp reaction fronts, facilitated by porosity creation because of the crystallisation of new phases, into less deformed older porphyroblast is common in exhumed eclogite facies rocks (Putnis and Austrheim 2010; Konrad-Schmolke et al. 2011). These processes also explain the gradual decrease in grainsizes of the amphibole constituting the symplectite, which occur as narrow bands across the omphacite, towards the remnant fragments of the omphacite (Fig. 2i,l). The linear nature and parallel faces (the symplectite-omphacite interfaces on either side of the band) of these symplectitic bands across omphacite and the presence of unfilled fractures along the short axes of some of the omphacite grains (Fig. 2c,d) suggest that symplectitisation progressed along omphacite fractures. The coarser amphibole grains (Fig. 2i,l) are also arranged linearly parallel to the short axis of the omphacite grain and most likely represent the core of the fracture. Therefore, we infer that the microfractures in some omphacite grains were pivotal in facilitating their complete symplectitisation, which further confirms that the studied symplectite in the eclogite was porous. They allowed the fluid to pass through and react with the pristine faces of the omphacite grains they mantled because, otherwise, the eclogite would have lacked both partially (Fig. 2i) and completely (Fig. 2j) symplectitised omphacites. Our inferences, unlike those of Marti *et al.* (2018) and Zertani *et al.* (2024), agree with the experimental demonstrations of a simultaneous increase in both porosity and volume during pseudomorphic replacements (Putnis et al. 2007; Xia et al. 2009).

5.3 Deformation of the garnet amphibolites

5.3.1 Amphibole

The strong CPOs of amphibole in both the garnet amphibolite samples (Fig. 7c,g) suggest they are well-deformed in the plastic regime. However, the effect of the shape-preferred orientations of the amphibole grains of sample 20-2 (Fig. 3a–c) on its CPO cannot be negated entirely. Although the large misfits between the random-pair and theoretical MADs of amphibole (Fig. 10e,f) could be a consequence of their clustered CPOs (Wheeler et al. 2001), the prominent subgrain boundaries (Fig. 14) support their intracrystalline deformation via the dislocation creep mechanism. The higher frequencies of the neighbour-pair misorientations at lower misorientation angles (10–<50°) than that expected from a uniform distribution means that the adjacent grains are similarly oriented (Fig. 10e,f), which could either be an effect of the clustered CPO or imply subgrain rotation recrystallisation of the amphibole grains (Trimby et al. 1998; Wheeler et al. 2001). Strong ductile deformation of the amphiboles in both the garnet amphibolites is evident, nonetheless. The non-random distributions of their LAXs with respect to the crystallographic axes (Fig. 9c,f) also confirm the same (Díaz Aspiroz et al. 2007). The distribution of the LAXs of amphibole in sample 20-2 shows a maximum that is nearly perpendicular to the (100) and (-100) planes with a sub-maximum parallel to the <001> axes. Assuming tilt subgrain boundaries, which require the slip direction and the misorientation axis to be perpendicular and parallel, respectively, to the subgrain walls (Lloyd et al. 1997; Dutta et al. 2022), the former arrangement of LAXs could imply the dominance of either <001>(010) or <010>(001) slip systems. The cluster of LAXs parallel to <001> axes would imply activities of either <010>(100) or <201>(010) slip systems. In the case of the amphibole of sample 19-8B, the spread of their LAXs along the (100) plane and the maxima parallel to the <001> axes suggest either <010>(100) or <100>(010) to be the active slip systems. Amongst these, both <001>(010) and <100>(010) have been previously identified (Morrison-Smith 1976; Reynard et al. 1989; Skrotzki 1992; Díaz Aspiroz et al. 2007), but <010>(100) is documented as a *‘hard’* slip system and difficult to trigger in naturally deformed amphiboles (Elyaszadeh et al. 2018). Additionally, the clustering of amphibole intragrain misorientation axes around their <001> axes has also been attributed to microfracturing and minute rigid body rotations (Soret et al. 2019; Jung et al. 2021). But since dislocation creep activity in the amphibole grains cannot be refuted given the prominent subgrain boundaries detected by the EBSD analysis (Fig. 14), we propose that the cluster of amphibole LAXs parallel to their c-axes in both the amphibolites could have resulted due to simultaneous operation multiple slip systems (Díaz Aspiroz et al. 2007).

Although intracrystalline plastic deformation and subgrain formation in amphibole is essentially reported for temperatures above 600 °C (Skrotzki 1990, 1992; Berger and Stünitz 1996; Díaz Aspiroz et al. 2007; Cao et al. 2010), subgrains have also been observed in amphibole grains deformed naturally in the temperature range 450–600 °C (Reynard et al. 1989; Elyaszadeh et al. 2018). The pressures predicted by these authors range between 4–7 kbar. Therefore, we propose 450 °C as the minimum temperature at which the garnet amphibolites experienced plastic strain. The $^{C}(Al+Fe^{3+}+Ti)$ + $^{A}(Na+K)$ and ^{T}Al contents of amphibole of the garnet amphibolite samples are higher than those of the symplectitic amphiboles in the eclogite sample 17-6C (Fig. 4d), implying that they equilibrated at higher temperatures than the latter (Nyman and Tracy 1993; Díaz Aspiroz et al. 2007; Cao et al. 2010). Furthermore, higher Al occupancy at the tetrahedral sites than the octahedral sites (Fig. SF7 in Supplementary File S1) and lower Na occupancy at the B sites (Fig. 4c) (which is also similar to those of the symplectitic amphiboles) also confirm their equilibration at low-pressure conditions (Brown 1977; Spear 1981, 1993; Palin et al. 2014).

5.3.2 Quartz

The quartz grains in both EBSD-mapped regions exhibit weak, nearly random CPOs (Fig. 7d,h) and lack subgrain boundaries. Although subgrains are present, they are limited to only a few coarse quartz grains in the thin sections (Figs 2e,f and 3b,f). These observations imply that quartz deformed at temperatures higher than 280 °C (Stipp et al. 2002), which caused some to develop strain-induced subgrains. Pervasive subgrain development in quartz at higher temperatures could have been limited because the thicker amphibole layers absorbed the strain (e.g., Tatham et al., 2008), whereas at lower temperatures, the strain rate was not high enough to trigger dislocation creep processes (Passchier and Trouw 2005).

5.4 Deformation v/s metamorphic reactions

Omphacite breakdown in eclogites typically produces rheologically weaker diopside-plagioclase symplectites, which, in the presence of aqueous fluids, further transform into amphibole-plagioclase symplectites under amphibolite facies conditions (Martin 2019). Replacement reactions such as the ones producing symplectite are typically characterised by a reduction of bulk strength (reaction weakening) and grainsizes (Marti et al. 2018; Mansard et al. 2020; Zertani et al. 2024). Therefore, syn-metamorphic deformation of the reaction products progresses via grainsize sensitive creep mechanisms, viz. diffusion or dissolution-precipitation creep (McNamara et al. 2024; Zertani et al. 2024). Although rare, cases of grainsize insensitive or dislocation creep are also reported for symplectite (Odashima et al. 2007; Zhao et al. 2012; Doi et al. 2014). Intracrystalline deformation, accommodated by dislocation motion, of the products of mineral transformation and replacement, particularly those that are inherently weaker, such as the plagioclase and amphibole, than their parents, can be triggered by the stress perturbations arising out of the volume increase resulting from the replacement reactions during retrogression (Greenwood and Johnson 1965; White and Knipe 1978; Poirier 1982, 1985; Brodie and Rutter 1985). Therefore, it is likely that despite their granular nature, the plagioclase and amphibole grains in the studied symplectite complexes deformed via dislocation creep.

The symplectite complexes investigated in this work consist of amphibole and plagioclase intergrowths, with a few grains of diopside, suggesting that the abundant amphibole crystals have most likely formed due to hydrous replacement of the earlier formed diopside grains. The two varieties of symplectites, S1 and S2, which we examined using EBSD, are symplectitised to varied extents, i.e., the latter contains no omphacite and a greater proportion of amphibole grains. We inferred (Sec. 5.2) this characteristic to be the consequence of heterogeneous distribution of the aqueous fluid in the eclogite because of its heterogeneous permeability (Fig. 15a–g). We further propose that the observed differences in the deformation mechanisms of plagioclase comprising the symplectites of Site 1S-A (type

S1) and Site 2S (type S2) also resulted from the heterogeneous fluid distribution. Limited availability of hydrous fluid at Site 1S-A, coupled with increased stresses at the omphacite-symplectite interface (Fig. 15h), allowed the development of subgrain structures via dislocation activity in the weaker plagioclase grains even in the presence of the diopside grains (Greenwood and Johnson 1965; Kenkmann and Dresen 1998). The amphibole grains (Amph-S1) that replaced the diopsides later also deformed in the dislocation creep regime for the same reasons. Elevated stresses at the omphacite-symplectite interface also explain the subgrain boundaries in the plagioclase and amphibole grains adjacent to the omphacite crystal in Site 1S-A (Figs 11a and 12a).

In contrast, decoupling between the precursor omphacite and the symplectite of Site 2S, due to the relatively higher supply of hydrous fluid (Fig. 15i), inhibited stress concentrations around the omphacite (Kenkmann and Dresen 1998) and, consequently, the plagioclase grains deformed via diffusion creep accommodated grain boundary sliding, which randomized their HAXs (Fig. 8i,j) (Jiang et al. 2000; Svahnberg and Piazolo 2010). The randomly distributed HAXs (Fig. 8e) suggest that the amphibole grains of Site 2S also experienced grain boundary sliding, which was accommodated by dislocation motion instead and, consequently, produced the low-angle boundaries seen in the coarser crystals (Fig. 13d–f). We further propose that, owing to the relatively greater proportion in both Site 1S-A and Site 2S compared to the plagioclase grains, the amphibole grains behaved as the load-bearing framework and continued to deform plastically by absorbing most of the strain (Brodie and Rutter 1985) even after the cessation of fluid ingress and symplectitisation.

6. Conclusions

Symplectite complexes are products of transformation/replacement reactions formed during retrogressive metamorphism. Diopside-plagioclase symplectite commonly originates in (U)HP eclogites due to decompression-induced destabilisation of omphacite. Subsequent hydration of the diopside component produces amphibole-plagioclase symplectite. Partial breakdown of omphacite to amphibole-plagioclase symplectite can also occur due to late-stage hydrous fluid influx. We investigated the deformation and mineralogical characteristics of the omphacite, amphibole-plagioclase symplectite, and the matrix components (amphibole and quartz) of an eclogite sample from the (U)HP Tso Morari region in the northwestern Indian Himalaya. We focused on the two varieties of symplectite, which replaced the omphacites partly along their peripheries (S1 symplectite) and completely (S2 symplectite). Albeit rare, fine diopside (Na = 0.18–0.25 apfu) is present in both S1 and S2, suggesting that amphibole replaced most of the precursor diopside during late-stage hydration. The omphacite grains (Na = 0.53–0.57 apfu) generally contain fractures, most of which are filled with symplectite. These fractures preferentially originated along the traces of the (100) cleavages due to the stress perturbations generated by the volume increase associated with symplectitisation and the localised overpressure generated by the fluids. The omphacite grains are chemically unzoned and devoid of subgrains, suggesting that they deformed via the body diffusion creep, which also resulted in their anisotropic and elliptical shapes. The consequent strong CPOs are inherited by amphibole and plagioclase constituting the symplectites (both S1 and S2) such that <001>$_{\mathrm{Omp}}$//<001>$_{\mathrm{Amp}}$//<010>$_{\mathrm{Plag}}$, <010>$_{\mathrm{Omp}}$//<010>$_{\mathrm{Amp}}$, and <100>$_{\mathrm{Omp}}$//<100>$_{\mathrm{Amp}}$//<001>$_{\mathrm{Plag}}$. The amphiboles in S1 (Amph-S1) are poorer in Si (6.75–7.34 apfu) compared to those in S2 (Amph-S2; Si = 7.29–7.79 apfu), demonstrating crystallisation of Amph-S2 at lower temperatures than Amph-S1 during retrogression. The heterogeneous distribution of the hydrous fluid, because of the heterogeneous permeability in the eclogite, was responsible for the varied degrees of symplectitisation. Relatively lower fluid supplies to S1 and elevated stresses at the omphacite-symplectite interface allowed the plagioclase grains to deform via dislocation activity, with <201>(010) and <001>(010) as the probable slip systems. In contrast, due to greater fluid availability, the plagioclase in S2 deformed via diffusion creep accommodated grain boundary sliding. Subgrain walls, with misorientations (4–9°) comparable to those observed in the amphiboles of the eclogite matrix and garnet amphibolites, are present in some of the coarser Amph-S1 and Amph-S2 grains, suggesting dislocation activity. The LAX distribution of the Amph-S1 grains is consistent with the known <001>(100) slip system for amphiboles, which is also predicted for those in the eclogite matrix. In contrast, the Amph-S2 grains deformed via grain boundary sliding, accommodated by dislocation creep. These characteristics suggest that plastic deformation of the amphiboles continued till the eclogite and garnet amphibolites reached depths corresponding to <10 kbar pressure, which also agrees with the lower Na occupancies (<1.0 apfu) at their B-sites.

Data availability

The EBSD data used in this study can be accessed from Zenodo Data Repository (https://doi.org/10.5281/zenodo.14776239). Representative mineral chemistry data are provided in the Electronic Supplementary Material file S1.

Acknowledgements

Dripta and Takeshi acknowledge the Postdoctoral Research Fellowship (23KF0120) and Grant-in-Aid Scientific Research Grant (23K22595), respectively, awarded by the Japan Society for the Promotion of Science (JSPS).

References

Ahmad T, Bhat IM, Tanaka T, et al (2022) Tso Morari Eclogites, Eastern Ladakh: Isotopic and Elemental Constraints on Their Protolith, Genesis, and Tectonic Setting. J Geol 130:231–252. https://doi.org/10.1086/719333

Allard M, Ildefonse B, Oliot É, Barou F (2021) Plastic Deformation of Plagioclase in Oceanic Gabbro Accreted at a Slow-Spreading Ridge (Hole U1473A, Atlantis Bank, Southwest Indian Ridge). J Geophys Res Solid Earth 126:. https://doi.org/10.1029/2021JB021964

Altenberger U, Wilhelm S (2000) Ductile deformation of K-feldspar in dry eclogite facies shear zones in the Bergen Arcs, Norway. Tectonophysics 320:107–121. https://doi.org/10.1016/S0040-1951(00)00048-2

Anderson ED, Moecher DP (2007) Omphacite breakdown reactions and relation to eclogite exhumation rates. Contrib Mineral Petrol 154:253–277. https://doi.org/10.1007/s00410-007-0192-x

Angiboust S, Pettke T, De Hoog JCM, et al (2014) Channelized Fluid Flow and Eclogite-facies Metasomatism along the Subduction Shear Zone. J Petrol 55:883–916. https://doi.org/10.1093/petrology/egu010

Bachmann F, Hielscher R, Schaeben H (2011) Grain detection from 2d and 3d EBSD data—Specification of the MTEX algorithm. Ultramicroscopy 111:1720–1733. https://doi.org/10.1016/j.ultramic.2011.08.002

Baëta RD, Ashbee KHG (1969) Slip systems in quartz: I. Experiments. Am Mineral 54:1551–1573

Baïsset M, Labrousse L, Schubnel A, et al (2024) Rheology of hydrated plagioclase at lower crustal conditions: Cataclasis, creep and transformational plasticity. J Struct Geol 178:105010. https://doi.org/10.1016/j.jsg.2023.105010

Baratoux L, Schulmann K, Ulrich S, Lexa O (2005) Contrasting microstructures and deformation mechanisms in metagabbro mylonites contemporaneously deformed under different temperatures (c. 650 °C and c. 750 °C). In: Gapais D, Brun JP, Cobbold PR (eds) Deformation Mechanisms, Rheology and Tectonics: from Minerals to the Lithosphere. Geological Society of London Special Publications. pp 97–125

Barker AJ (1998) Mineral inclusions, intergrowths and coronas. In: Introduction to Metamorphic Textures and Microstructures. Stanley Thomes (Publishers) Ltd, Cheltenham, United Kingdom, pp 85–100

Berger A, Stünitz H (1996) Deformation mechanisms and reaction of hornblende: examples from the Bergell tonalite (Central Alps). Tectonophysics 257:149–174. https://doi.org/10.1016/0040-1951(95)00125-5

Bestmann M, Piazolo S, Spiers CJ, Prior DJ (2005) Microstructural evolution during initial stages of static recovery and recrystallization: new insights from in-situ heating experiments combined with electron backscatter diffraction analysis. J Struct Geol 27:447–457. https://doi.org/10.1016/j.jsg.2004.10.006

Bidgood AK, Parsons AJ, Lloyd GE, et al (2021) EBSD-based criteria for coesite-quartz transformation. J Metamorph Geol 39:165–180. https://doi.org/10.1111/jmg.12566

Bidgood AK, Waters DJ, Dyck BJ, Roberts NMW (2023) The emplacement, alteration, subduction and metamorphism of metagranites from the Tso Morari Complex, Ladakh Himalaya. Mineral Mag 87:40–59. https://doi.org/10.1180/mgm.2022.121

Biermann C, Van Roermund HLM (1983) Defect structures in naturally deformed clinoamphiboles—a TEM study. Tectonophysics 95:267–278. https://doi.org/10.1016/0040-1951(83)90072-0

Boland JN, Van Roermund HLM (1983) Mechanisms of exsolution in omphacites from high temperature, type B, eclogites. Phys Chem Miner 9:30–37. https://doi.org/10.1007/BF00309467

Brander L, Svahnberg H, Piazolo S (2012) Brittle-plastic deformation in initially dry rocks at fluid-present conditions: transient behaviour of feldspar at mid-crustal levels. Contrib Mineral Petrol 163:403–425. https://doi.org/10.1007/s00410-011-0677-5

Brenker FE, Prior DJ, Müller WF (2002) Cation ordering in omphacite and effect on deformation mechanism and lattice preferred orientation (LPO). J Struct Geol 24:1991–2005. https://doi.org/10.1016/S0191-8141(02)00010-X

Brodie KH (1995) The development of orientated symplectites during deformation. J Metamorph Geol 13:499–508. https://doi.org/10.1111/j.1525-1314.1995.tb00237.x

Brodie KH, Rutter EH (1987) The role of transiently fine-grained reaction products in syntectonic metamorphism: natural and experimental examples. Can J Earth Sci 24:556–564. https://doi.org/10.1139/e87-054

Brodie KH, Rutter EH (1985) On the Relationship between Deformation and Metamorphism, with Special Reference to the Behavior of Basic Rocks. In: Thompson AB, Rubie DC (eds) Metamorphic Reactions. Springer New York, New York, NY, pp 138–179

Brown EH (1977) The Crossite Content of Ca-Amphibole as a Guide to Pressure of Metamorphism. J Petrol 18:53–72. https://doi.org/10.1093/petrology/18.1.53

Buchs N, Epard J-L (2019) Geology of the eastern part of the Tso Morari nappe, the Nidar Ophiolite and the surrounding tectonic units (NW Himalaya, India). J Maps 15:38–48. https://doi.org/10.1080/17445647.2018.1541196

Cao S, Liu J, Leiss B (2010) Orientation-related deformation mechanisms of naturally deformed amphibole in amphibolite mylonites from the Diancang Shan, SW Yunnan, China. J Struct Geol 32:606–622. https://doi.org/10.1016/j.jsg.2010.03.012

Cao Y, Du J, Park M, et al (2020) Metastability and Nondislocation-Based Deformation Mechanisms of the Flem Eclogite in the Western Gneiss Region, Norway. J Geophys Res Solid Earth 125:e2020JB019375. https://doi.org/10.1029/2020JB019375

Cao Y, Song SG, Niu YL, et al (2011) Variation of mineral composition, fabric and oxygen fugacity from massive to foliated eclogites during exhumation of subducted ocean crust in the North Qilian suture zone, NW China. J Metamorph Geol 29:699–720. https://doi.org/10.1111/j.1525-1314.2011.00937.x

Carter NL, Kronenberg AK, Ross JV, Wiltschko DV (1990) Control of fluids on deformation of rocks. In: Knipe RJ, Rutter EH (eds) Deformation Mechanisms, Rheology and Tectonics. Geological Society of London Special Publications. pp 1–13

Chatterjee A, Daczko NR, Dey J, Piazolo S (2024) Hydrous shear zones are sites of melt transfer in the lower arc crust: A case study from Fiordland, New Zealand. J Metamorph Geol 42:933–956. https://doi.org/10.1111/jmg.12788

Chatterjee N, Jagoutz O (2015) Exhumation of the UHP Tso Morari eclogite as a diapir rising through the mantle wedge. Contrib Mineral Petrol 169:3. https://doi.org/10.1007/s00410-014-1099-y

Cox SF, Etheridge MA (1989) Coupled grain-scale dilatancy and mass transfer during deformation at high fluid pressures: examples from Mount Lyell, Tasmania. J Struct Geol 11:147–162. https://doi.org/10.1016/0191-8141(89)90040-0

Crameri F (2018) Scientific colour maps

de Sigoyer J, Guillot S, Dick P (2004) Exhumation of the ultrahigh-pressure Tso Morari unit in eastern Ladakh (NW Himalaya): A case study. Tectonics 23:1–18. https://doi.org/10.1029/2002TC001492

de Sigoyer J, Guillot S, Lardeaux J-M, Mascle G (1997) Glaucophane-bearing eclogites in the Tso Morari dome (eastern Ladakh, NW Himalaya). Eur J Mineral 9:1073–1084. https://doi.org/10.1127/ejm/9/5/1073

Deer WA, Howie RA, Zussman J (2013) An Introduction to the Rock-Forming Minerals, Third. Mineralogical Society of Great Britain and Ireland, UK

Dey A, Sen K, Mamtani MA (2022) Electron Backscatter Diffraction Study of Ultrahigh-Pressure Tso Morari Eclogites (Trans-Himalayan Collisional Zone): Implications for Strain Regime Transition from Constrictional to Plane Strain during Exhumation. Lithosphere 2022:7256746. https://doi.org/10.2113/2022/7256746

Dey A, Sen K, Sen A, Choudhary S (2023) Omphacite breakdown, symplectite formation and carbonate metasomatism in a retrograded continental eclogite: Implications for the exhumation of the Tso Morari Crystalline Complex (Trans-Himalaya, NW India). Phys Chem Earth Parts ABC 131:103453. https://doi.org/10.1016/j.pce.2023.103453

Di Vincenzo G, Palmeri R (2001) An 40Ar–39Ar investigation of high-pressure metamorphism and the retrogressive history of mafic eclogites from the Lanterman Range (Antarctica): evidence against a simple temperature control on argon transport in amphibole. Contrib Mineral Petrol 141:15–35. https://doi.org/10.1007/s004100000226

Díaz Aspiroz M, Lloyd GE, Fernández C (2007) Development of lattice preferred orientation in clinoamphiboles deformed under low-pressure metamorphic conditions. A SEM/EBSD study of metabasites from the Aracena metamorphic belt (SW Spain). J Struct Geol 29:629–645. https://doi.org/10.1016/j.jsg.2006.10.010

Dimanov A, Dresen G (2005) Rheology of synthetic anorthite-diopside aggregates: Implications for ductile shear zones. J Geophys Res Solid Earth 110:. https://doi.org/10.1029/2004JB003431

Doi N, Kato T, Kubo T, et al (2014) Creep behavior during the eutectoid transformation of albite: Implications for the slab deformation in the lower mantle. Earth Planet Sci Lett 388:92–97. https://doi.org/10.1016/j.epsl.2013.09.009

Dollinger G, Blacic JD (1975) Deformation mechanisms in experimentally and naturally deformed amphiboles. Earth Planet Sci Lett 26:409–416. https://doi.org/10.1016/0012-821X(75)90016-3

Droop GTR (1987) A general equation for estimating Fe3+ concentrations in ferromagnesian silicates and oxides from microprobe analyses, using stoichiometric criteria. Mineral Mag 51:431–435. https://doi.org/10.1180/minmag.1987.051.361.10

Dutta D, Misra S, Karmakar S (2022) Deformation mechanisms and characteristics of the meta-BIFs from an early Proterozoic shear system of the Southern Granulite Terrane (SGT), India. J Struct Geol 156:104534. https://doi.org/10.1016/j.jsg.2022.104534

Dutta D, Mukherjee S (2021) Extrusion kinematics of UHP terrane in a collisional orogen: EBSD and microstructure-based approach from the Tso Morari Crystallines (Ladakh Himalaya). Tectonophysics 800:228641. https://doi.org/10.1016/j.tecto.2020.228641

Elyaszadeh R, Prior DJ, Sarkarinejad K, Mansouri H (2018) Different slip systems controlling crystallographic preferred orientation and intracrystalline deformation of amphibole in mylonites from the Neyriz mantle diapir, Iran. J Struct Geol 107:38–52. https://doi.org/10.1016/j.jsg.2017.11.020

Engvik AK, Austrheim H, Erambert M (2001) Interaction between fluid flow, fracturing and mineral growth during eclogitization, an example from the Sunnfjord area, Western Gneiss Region, Norway. Lithos 57:111–141. https://doi.org/10.1016/S0024-4937(01)00037-8

Epard J-L, Steck A (2008) Structural development of the Tso Morari ultra-high pressure nappe of the Ladakh Himalaya. Tectonophysics 451:242–264. https://doi.org/10.1016/j.tecto.2007.11.050

Ferry JM (1994) A historical review of metamorphic fluid flow. J Geophys Res Solid Earth 99:15487–15498. https://doi.org/10.1029/94JB01147

Fukuda J, Muto J, Koizumi S, et al (2022) Enhancement of ductile deformation in polycrystalline anorthite due to the addition of water. J Struct Geol 156:104547. https://doi.org/10.1016/j.jsg.2022.104547

Fukuda J, Okudaira T (2013) Grain-size-sensitive creep of plagioclase accompanied by solution–precipitation and mass transfer under mid-crustal conditions. J Struct Geol 51:61–73. https://doi.org/10.1016/j.jsg.2013.03.006

Gaidies F, Milke R, Heinrich W, Abart R (2017) Metamorphic mineral reactions: Porphyroblast, corona and symplectite growth. In: Heinrich W, Abart R (eds) Mineral reaction kinetics: Microstructures, textures, chemical and isotopic signatures. European Mineralogical Union and Mineralogical Society of Great Britain and Ireland, p 0

García-Casco A, Torres-Roldán RL (1996) Disequilibrium Induced by Fast Decompression in St−Bt−Grt−Ky−Sil−And Metapelites from the Betic Belt (Southern Spain). J Petrol 37:1207–1239. https://doi.org/10.1093/petrology/37.5.1207

Girard M, Bussy F (1999) Late Pan-African magmatism in the Himalaya : new geochronological and geochemical data from the Ordovician Tso Morari metagranites (Ladakh, NW India). Schweiz Mineral Petrogr Mitteilungen 79:399–418. https://doi.org/10.5169/SEALS-60215

Godard G, Van Roermund HLM (1995) Deformation-induced clinopyroxene fabrics from eclogites. J Struct Geol 17:1425–1443. https://doi.org/10.1016/0191-8141(95)00038-F

Greenwood GW, Johnson RH (1965) The deformation of metals under small stresses during phase transformations. Proc R Soc Lond Ser Math Phys Sci 283:403–422. https://doi.org/10.1098/rspa.1965.0029

Groppo C, Lombardo B, Castelli D, Compagnoni R (2007) Exhumation History of the UHPM Brossasco-Isasca Unit, Dora-Maira Massif, as Inferred from a Phengite-Amphibole Eclogite. Int Geol Rev 49:142–168. https://doi.org/10.2747/0020-6814.49.2.142

Guillot S, de Sigoyer J, Lardeaux JM, Mascle G (1997) Eclogitic metasediments from the Tso Morari area (Ladakh, Himalaya): evidence for continental subduction during India-Asia convergence. Contrib Mineral Petrol 128:197–212. https://doi.org/10.1007/s004100050303

Hacker BR, Christie JM (1990) Brittle/Ductile and Plastic/Cataclastic Transitions in Experimentally Deformed and Metamorphosed Amphibolite. In: Duba AG, Durham WB, Handin JW, Wang HF (eds) The Brittle-Ductile Transition in Rocks. American Geophysical Union (AGU), pp 127–147

Hawthorne FC, Oberti R, Harlow GE, et al (2012) Nomenclature of the amphibole supergroup. Am Mineral 97:2031–2048. https://doi.org/10.2138/am.2012.4276

Heidelbach F, Terry MP (2013) Inherited Fabric in an Omphacite Symplectite: Reconstruction of Plastic Deformation under Ultra-High Pressure Conditions. Microsc Microanal 19:942–949. https://doi.org/10.1017/S1431927613001451

Hielscher R, Schaeben H (2008) A novel pole figure inversion method: specification of the *MTEX* algorithm. J Appl Crystallogr 41:1024–1037. https://doi.org/10.1107/S0021889808030112

Hirth G, Tullis J (1992) Dislocation creep regimes in quartz aggregates. J Struct Geol 14:145–159. https://doi.org/10.1016/0191-8141(92)90053-Y

Imayama T, Dutta D, Yi K (2024) The origin of the ultrahigh-pressure Tso Morari complex, NW Himalaya: implication for early Paleozoic rifting. Geol Mag 1–8. https://doi.org/10.1017/S0016756824000025

Imayama T, Oh C-W, Baltybaev SK, et al (2017) Paleoproterozoic high-pressure metamorphic history of the Salma eclogite on the Kola Peninsula, Russia. Lithosphere 9:855–873. https://doi.org/10.1130/L657.1

Jamtveit B, Austrheim H, Putnis A (2016) Disequilibrium metamorphism of stressed lithosphere. Earth-Sci Rev 154:1–13. https://doi.org/10.1016/j.earscirev.2015.12.002

Jamtveit B, Malthe-Sørenssen A, Kostenko O (2008) Reaction enhanced permeability during retrogressive metamorphism. Earth Planet Sci Lett 267:620–627. https://doi.org/10.1016/j.epsl.2007.12.016

Jamtveit B, Putnis CV, Malthe-Sørenssen A (2009) Reaction induced fracturing during replacement processes. Contrib Mineral Petrol 157:127–133. https://doi.org/10.1007/s00410-008-0324-y

Ji S, Mainprice D (1990) Recrystallization and Fabric Development in Plagioclase. J Geol 98:65–79

Jiang Z, Prior DJ, Wheeler J (2000) Albite crystallographic preferred orientation and grain misorientation distribution in a low-grade mylonite: implications for granular flow. J Struct Geol 22:1663–1674. https://doi.org/10.1016/S0191-8141(00)00079-1

Joanny V, Van Roermund H, Lardeaux JM (1991) The clinopyroxene/plagioclase symplectite in retrograde eclogites: A potential geothermobarometer. Geol Rundsch 80:303–320. https://doi.org/10.1007/BF01829368

Jonas L, John T, King HE, et al (2014) The role of grain boundaries and transient porosity in rocks as fluid pathways for reaction front propagation. Earth Planet Sci Lett 386:64–74. https://doi.org/10.1016/j.epsl.2013.10.050

Jonnalagadda MK, Karmalkar NR, Duraiswami RA (2019) Geochemistry of eclogites of the Tso Morari complex, Ladakh, NW Himalayas: Insights into trace element behavior during subduction and exhumation. Geosci Front 10:811–826. https://doi.org/10.1016/j.gsf.2017.05.013

Jung S, Yamamoto T, Ando J, Jung H (2021) Dislocation Creep of Olivine and Amphibole in Amphibole Peridotites from Åheim, Norway. Minerals 11:1018. https://doi.org/10.3390/min11091018

Kelemen PB, Hirth G (2012) Reaction-driven cracking during retrograde metamorphism: Olivine hydration and carbonation. Earth Planet Sci Lett 345–348:81–89. https://doi.org/10.1016/j.epsl.2012.06.018

Kenkmann T, Dresen G (1998) Stress gradients around porphyroclasts: palaeopiezometric estimates and numerical modelling. J Struct Geol 20:163–173. https://doi.org/10.1016/S0191-8141(97)00074-6

Keppler R, Stipp M, Behrmann JH, et al (2016) Deformation inside a paleosubduction channel – Insights from microstructures and crystallographic preferred orientations of eclogites and metasediments from the Tauern Window, Austria. J Struct Geol 82:60–79. https://doi.org/10.1016/j.jsg.2015.11.006

Ko B, Jung H (2015) Crystal preferred orientation of an amphibole experimentally deformed by simple shear. Nat Commun 6:6586. https://doi.org/10.1038/ncomms7586

Konrad-Schmolke M, O’Brien PJ, Zack T (2011) Fluid Migration above a Subducted Slab—Constraints on Amount, Pathways and Major Element Mobility from Partially Overprinted Eclogite-facies Rocks (Sesia Zone, Western Alps). J Petrol 52:457–486. https://doi.org/10.1093/petrology/egq087

Kruse R, Stünitz H (1999) Deformation mechanisms and phase distribution in mafic high-temperature mylonites from the Jotun Nappe, southern Norway. Tectonophysics 303:223–249. https://doi.org/10.1016/S0040-1951(98)00255-8

Kruse R, Stünitz H, Kunze K (2001) Dynamic recrystallization processes in plagioclase porphyroclasts. J Struct Geol 23:1781–1802. https://doi.org/10.1016/S0191-8141(01)00030-X

Lanari P, Riel N, Guillot S, et al (2013) Deciphering high-pressure metamorphism in collisional context using microprobe mapping methods: Application to the Stak eclogitic massif (northwest Himalaya). Geology 41:111–114. https://doi.org/10.1130/G33523.1

Leake BE, Woolley AR, Arps CES, et al (1997) Nomenclature of amphiboles; report of the subcommittee on amphiboles of the International Mineralogical Association, Commission on New Minerals and Mineral Names. Can Mineral 35:219–246

Lianxing G, Jianguo D, Jianping Z, et al (2002) Eclogites of the Dabie Region: Retrograde Metamorphism and Fluid Evolution. Acta Geol Sin - Engl Ed 76:166–182. https://doi.org/10.1111/j.1755-6724.2002.tb00083.x

Liu J, Cao S (2023) Development of Amphibole Crystal Preferred Orientations (CPOs) and Their Effects on Seismic Anisotropy in Deformed Amphibolites. J Geophys Res Solid Earth 128:e2022JB026136. https://doi.org/10.1029/2022JB026136

Liu Q, Hermann J, Zhang J (2013) Polyphase inclusions in the Shuanghe UHP eclogites formed by subsolidus transformation and incipient melting during exhumation of deeply subducted crust. Lithos 177:91–109. https://doi.org/10.1016/j.lithos.2013.06.010

Lloyd GE (2004) Microstructural evolution in a mylonitic quartz simple shear zone: the significant roles of dauphine twinning and misorientation. Flow Process Faults Shear Zones Geol Soc Lond Spec Publ 224:39–61. https://doi.org/10.1144/GSL.SP.2004.224.01.04

Lloyd GE, Farmer AB, Mainprice D (1997) Misorientation analysis and the formation and orientation of subgrain and grain boundaries. Tectonophysics 279:55–78. https://doi.org/10.1016/S0040-1951(97)00115-7

Long SP, Kohn MJ, Kerswell BC, et al (2020) Thermometry and Microstructural Analysis Imply Protracted Extensional Exhumation of the Tso Morari UHP Nappe, Northwestern Himalaya: Implications for Models of UHP Exhumation. Tectonics 39:e2020TC006482. https://doi.org/10.1029/2020TC006482

Mansard N, Stünitz H, Raimbourg H, et al (2020) Relationship between microstructures and resistance in mafic assemblages that deform and transform. Solid Earth 11:2141–2167. https://doi.org/10.5194/se-11-2141-2020

Marti S, Stünitz H, Heilbronner R, et al (2018) Syn-kinematic hydration reactions, grain size reduction, and dissolution–precipitation creep in experimentally deformed plagioclase–pyroxene mixtures. Solid Earth 9:985–1009. https://doi.org/10.5194/se-9-985-2018

Martin C (2019) P-T conditions of symplectite formation in the eclogites from the Western Gneiss Region (Norway). In: Ferrero S, Lanari P, Goncalves P, Grosch EG (eds) Metamorphic Geology: Microscale to Mountain Belts. Geological Society of London Special Publications. pp 197–216

Martin C, Duchêne S (2015) Residual water in hydrous minerals as a kinetic factor for omphacite destabilization into symplectite in the eclogites of Vårdalsneset (WGR, Norway). Lithos 232:162–173. https://doi.org/10.1016/j.lithos.2015.06.021

Massonne H-J (2012) Formation of Amphibole and Clinozoisite–Epidote in Eclogite owing to Fluid Infiltration during Exhumation in a Subduction Channel. J Petrol 53:1969–1998. https://doi.org/10.1093/petrology/egs040

Mauler A, Godard G, Kunze K (2001) Crystallographic fabrics of omphacite, rutile and quartz in Vendée eclogites (Armorican Massif, France). Consequences for deformation mechanisms and regimes. Tectonophysics 342:81–112. https://doi.org/10.1016/S0040-1951(01)00157-3

McNamara DD, Wheeler J, Pearce M, Prior DJ (2012) Fabrics produced mimetically during static metamorphism in retrogressed eclogites from the Zermatt-Saas zone, Western Italian Alps. J Struct Geol 44:167–178. https://doi.org/10.1016/j.jsg.2012.08.006

McNamara DD, Wheeler J, Pearce M, Prior DJ (2024) A key role for diffusion creep in eclogites: Omphacite deformation in the Zermatt-Saas unit, Italian Alps. J Struct Geol 179:105033. https://doi.org/10.1016/j.jsg.2023.105033

Mindaleva D, Uno M, Higashino F, et al (2020) Rapid fluid infiltration and permeability enhancement during middle–lower crustal fracturing: Evidence from amphibolite–granulite-facies fluid–rock reaction zones, Sør Rondane Mountains, East Antarctica. Lithos 372–373:105521. https://doi.org/10.1016/j.lithos.2020.105521

Morimoto N (1989) Nomenclature of pyroxenes. Mineral J 14:198–221. https://doi.org/10.2465/minerj.14.198

Mørk MBE (1985) Incomplete high P–T metamorphic transitions within the Kvamsøy pyroxenite complex, west Norway: a case study of disequilibrium. J Metamorph Geol 3:245–264. https://doi.org/10.1111/j.1525-1314.1985.tb00320.x

Morrison-Smith DJ (1976) Transmission electron microscopy of experimentally deformed hornblende. Am Mineral 61:272–280

Mukherjee BK, Sachan HK, Ogasawara Y, et al (2003) Carbonate-Bearing UHPM Rocks from the Tso-Morari Region, Ladakh, India: Petrological Implications. Int Geol Rev 45:49–69. https://doi.org/10.2747/0020-6814.45.1.49

Nyman MW, Tracy RJ (1993) Petrological evolution of amphibolite shear zones, Cheyenne Belt, south-eastern Wyoming, USA. J Metamorph Geol 11:757–773. https://doi.org/10.1111/j.1525-1314.1993.tb00185.x

O’Brien PJ (1993) Partially retrograded eclogites of the Münchberg Massif, Germany: records of a multi-stage Variscan uplift history in the Bohemian Massif. J Metamorph Geol 11:241–260. https://doi.org/10.1111/j.1525-1314.1993.tb00145.x

Odashima N, Morishita T, Ozawa K, et al (2007) Formation and deformation mechanisms of pyroxene-spinel symplectite in an ascending mantle, the Horoman peridotite complex, Japan: An EBSD (electron backscatter diffraction) study. J Mineral Petrol Sci 103:1–15. https://doi.org/10.2465/jmps.070222b

Ogilvie P, Gibson RL (2017) Arrested development – a comparative analysis of multilayer corona textures in high-grade metamorphic rocks. Solid Earth 8:93–135. https://doi.org/10.5194/se-8-93-2017

Olsen TS, Kohlstedt DL (1984) Analysis of dislocations in some naturally deformed plagioclase feldspars. Phys Chem Miner 11:153–160. https://doi.org/10.1007/BF00387845

Olsen TS, Kohlstedt DL (1985) Natural deformation and recrystallization of some intermediate plagioclase feldspars. Tectonophysics 111:107–131. https://doi.org/10.1016/0040-1951(85)90067-8

Palin RM, Reuber GS, White RW, et al (2017) Subduction metamorphism in the Himalayan ultrahigh-pressure Tso Morari massif: An integrated geodynamic and petrological modelling approach. Earth Planet Sci Lett 467:108–119. https://doi.org/10.1016/j.epsl.2017.03.029

Palin RM, St-Onge MR, Waters DJ, et al (2014) Phase equilibria modelling of retrograde amphibole and clinozoisite in mafic eclogite from the Tso Morari massif, northwest

India: constraining the *P* - *T* - *M* (H_2O) conditions of exhumation. J Metamorph Geol 32:675–693. https://doi.org/10.1111/jmg.12085

Palmeri R, Chmielowski R, Sandroni S, et al (2009) Petrology of the eclogites from western Tasmania: Insights into the Cambro-Ordovician evolution of the paleo-Pacific margin of Gondwana. Lithos 109:223–239. https://doi.org/10.1016/j.lithos.2008.06.016

Pan R, Macris CA, Menold CA (2020) Thermodynamic modeling of high-grade metabasites: a case study using the Tso Morari UHP eclogite. Contrib Mineral Petrol 175:78. https://doi.org/10.1007/s00410-020-01717-w

Passchier CW, Trouw RAJ (eds) (2005) Deformation Mechanisms. In: Microtectonics. Springer, Berlin, Heidelberg, pp 25–66

Paterson MS, Wong T (eds) (2005) Experimental Studies on the Brittle Fracture Stress. In: Experimental Rock Deformation — The Brittle Field. Springer, Berlin, Heidelberg, pp 17–44

Pearce MA, Timms NE, Hough RM, Cleverley JS (2013) Reaction mechanism for the replacement of calcite by dolomite and siderite: implications for geochemistry, microstructure and porosity evolution during hydrothermal mineralisation. Contrib Mineral Petrol 166:995–1009. https://doi.org/10.1007/s00410-013-0905-2

Pennacchioni G (1996) Progressive eclogitization under fluid-present conditions of pre-Alpine mafic granulites in the Austroalpine Mt Emilius Klippe (Italian Western Alps). J Struct Geol 18:549–561. https://doi.org/10.1016/S0191-8141(96)80023-X

Peterman EM, Grove M (2010) Growth conditions of symplectic muscovite + quartz: Implications for quantifying retrograde metamorphism in exhumed magmatic arcs. Geology 38:1071–1074. https://doi.org/10.1130/G31449.1

Piepenbreier D, Stöckhert B (2001) Plastic flow of omphacite in eclogites at temperatures below 500°C – implications for interplate coupling in subduction zones. Int J Earth Sci 90:197–210. https://doi.org/10.1007/s005310000159

Poirier JP (1982) On transformation plasticity. J Geophys Res Solid Earth 87:6791–6797. https://doi.org/10.1029/JB087iB08p06791

Poirier J-P (ed) (1985) Transformation plasticity. In: Creep of Crystals: High-Temperature Deformation Processes in Metals, Ceramics and Minerals. Cambridge University Press, Cambridge, pp 213–228

Putnis A, Austrheim H (2010) Fluid-induced processes: metasomatism and metamorphism. Geofluids 10:254–269. https://doi.org/10.1111/j.1468-8123.2010.00285.x

Putnis CV, Geisler T, Schmid-Beurmann P, et al (2007) An experimental study of the replacement of leucite by analcime. Am Mineral 92:19–26. https://doi.org/10.2138/am.2007.2249

Rehman HU, Mainprice D, Barou F, et al (2016) EBSD-measured crystal preferred orientation of eclogites from the Sanbagawa metamorphic belt, central Shikoku, SW Japan. Eur J Mineral 28:1155–1168. https://doi.org/10.1127/ejm/2016/0028-2574

Renedo RN, Nachlas WO, Whitney DL, et al (2015) Fabric development during exhumation from ultrahigh-pressure in an eclogite-bearing shear zone, Western Gneiss Region, Norway. J Struct Geol 71:58–70. https://doi.org/10.1016/j.jsg.2014.09.012

Reynard B, Gillet P, Willaime C (1989) Deformation mechanisms in naturally deformed glaucophanes; a TEM and HREM study. Eur J Mineral 1:611–624

Robinson P, Ross M, Jaefe HW (1971) Composition of the Anthophyllite-Gedrite Series, Comparisons of Gedrite and Hornblende, and the Anthophyllite-Gedrite Solvus. Am Mineral 56:1005–1041

Rogowitz A, Huet B (2021) Evolution of fluid pathways during eclogitization and their impact on formation and deformation of eclogite: A microstructural and petrological investigation at the type locality (Koralpe, Eastern Alps, Austria). Tectonophysics 819:229079. https://doi.org/10.1016/j.tecto.2021.229079

Rooney TP, Riecker RE, Gavasci AT (1975) Hornblende deformation features. Geology 3:364–366. https://doi.org/10.1130/0091-7613(1975)3<364:HDF>2.0.CO;2

Rybacki E, Dresen G (2000) Dislocation and diffusion creep of synthetic anorthite aggregates. J Geophys Res Solid Earth 105:26017–26036. https://doi.org/10.1029/2000JB900223

Rybacki E, Dresen G (2004) Deformation mechanism maps for feldspar rocks. Tectonophysics 382:173–187. https://doi.org/10.1016/j.tecto.2004.01.006

Schmid SM, Casey M (1986) Complete fabric analysis of some commonly observed quartz c-axis patterns. Miner Rock Deform Lab Stud Geophys Monogr Ser 36:263–286. https://doi.org/10.1029/GM036p0263

Scott JM, Konrad-Schmolke M, O’brien PJ, Günter C (2013) High-T, Low-P Formation of Rare Olivine-bearing Symplectites in Variscan Eclogite. J Petrol 54:1375–1398. https://doi.org/10.1093/petrology/egt015

Shigematsu N, Tanaka H (2000) Dislocation creep of fine-grained recrystallized plagioclase under low-temperature conditions. J Struct Geol 22:65–79. https://doi.org/10.1016/S0191-8141(99)00132-7

Sikdar A, Dutta D, Misra S (2023) Superplastic deformation inside the knife-sharp shear bands in mid-crustal granites. J Struct Geol 177:104980. https://doi.org/10.1016/j.jsg.2023.104980

Skemer P, Katayama I, Jiang Z, Karato S (2005) The misorientation index: Development of a new method for calculating the strength of lattice-preferred orientation. Tectonophysics 411:157–167. https://doi.org/10.1016/j.tecto.2005.08.023

Skrotzki W (1992) Defect structure and deformation mechanisms in naturally deformed hornblende. Phys Status Solidi A 131:605–624. https://doi.org/10.1002/pssa.2211310232

Skrotzki W (1990) Microstructure in hornblende of a mylonitic amphibolite. In: Knipe RJ, Rutter EH (eds) Deformation Mechanisms, Rheology and Tectonics. Geological Society of London Special Publications. pp 321–325

Soret M, Agard P, Ildefonse B, et al (2019) Deformation mechanisms in mafic amphibolites and granulites: record from the Semail metamorphic sole during subduction infancy. Solid Earth 10:1733–1755. https://doi.org/10.5194/se-10-1733-2019

Spear FS (1981) An experimental study of hornblende stability and compositional variability in amphibolite. Am J Sci 281:697–734. https://doi.org/10.2475/ajs.281.6.697

Spear FS (1993) Metamorphic phase equilibria and pressure-temperature-time paths. Mineral Soc Am Monogr 799:

Spencer DA, Tonarini S, Pognante U (1995) Geochemical and Sr-Nd isotopic characterisation of Higher Himalayan eclogites (and associated metabasites). Eur J Mineral 89–102. https://doi.org/10.1127/ejm/7/1/0089

Spruzeniece L, Piazolo S, Daczko NR, et al (2017a) Symplectite formation in the presence of a reactive fluid: insights from hydrothermal experiments. J Metamorph Geol 35:281–299. https://doi.org/10.1111/jmg.12231

Spruzeniece L, Piazolo S, Maynard-Casely HE (2017b) Deformation-resembling microstructure created by fluid-mediated dissolution–precipitation reactions. Nat Commun 8:14032. https://doi.org/10.1038/ncomms14032

Spry A (1969) Metamorphic Textures. Pergamon

Stipp M, Stünitz H, Heilbronner R, Schmid SM (2002) The eastern Tonale fault zone: a ‘natural laboratory’ for crystal plastic deformation of quartz over a temperature range from 250 to 700°C. J Struct Geol 24:1861–1884. https://doi.org/10.1016/S0191-8141(02)00035-4

Štípská P, Powell R (2005) Constraining the P–T path of a MORB-type eclogite using pseudosections, garnet zoning and garnet-clinopyroxene thermometry: an example from the Bohemian Massif. J Metamorph Geol 23:725–743. https://doi.org/10.1111/j.1525-1314.2005.00607.x

Stöckhert B (2002) Stress and deformation in subduction zones: insight from the record of exhumed metamorphic rocks. In: De Meer S, Drury MR, de Bresser JHP, Pennock GM (eds) Deformation Mechanisms, Rheology and Tectonics: Current Status and Future Perspectives. Geological Society of London Special Publications. pp 255–274

St-Onge MR, Rayner N, Palin RM, et al (2013) Integrated pressure-temperature-time constraints for the Tso Morari dome (Northwest India): implications for the burial and exhumation path of UHP units in the western Himalaya. J Metamorph Geol 31:469–504. https://doi.org/10.1111/jmg.12030

Stout JH (1972) Phase Petrology and Mineral Chemistry of Coexisting Amphiboles from Telemark, Norway. J Petrol 13:99–145. https://doi.org/10.1093/petrology/13.1.99

Straume, Austrheim (1999) Importance of fracturing during retro-metamorphism of eclogites. J Metamorph Geol 17:637–652. https://doi.org/10.1046/j.1525-1314.1999.00218.x

Stünitz H, Neufeld K, Heilbronner R, et al (2020) Transformation weakening: Diffusion creep in eclogites as a result of interaction of mineral reactions and deformation. J Struct Geol 139:104129. https://doi.org/10.1016/j.jsg.2020.104129

Svahnberg H, Piazolo S (2010) The initiation of strain localisation in plagioclase-rich rocks: Insights from detailed microstructural analyses. J Struct Geol 32:1404–1416. https://doi.org/10.1016/j.jsg.2010.06.011

Tatham DJ, Lloyd GE, Butler RWH, Casey M (2008) Amphibole and lower crustal seismic properties. Earth Planet Sci Lett 267:118–128. https://doi.org/10.1016/j.epsl.2007.11.042

Tichomirowa M, Köhler R (2013) Discrimination of protolithic versus metamorphic zircon ages in eclogites: Constraints from the Erzgebirge metamorphic core complex (Germany). Lithos 177:436–450. https://doi.org/10.1016/j.lithos.2013.07.013

Trimby PW, Prior DJ, Wheeler J (1998) Grain boundary hierarchy development in a quartz mylonite. J Struct Geol 20:917–935. https://doi.org/10.1016/S0191-8141(98)00026-1

Tullis J, Yund RA (1980) Hydrolytic weakening of experimentally deformed Westerly granite and Hale albite rock. J Struct Geol 2:439–451. https://doi.org/10.1016/0191-8141(80)90005-X

Van Der Werf T, Chatzaras V, Kriegsman LM, et al (2017) Constraints on the rheology of the lower crust in a strike-slip plate boundary: evidence from the San Quintín xenoliths, Baja California, Mexico. Solid Earth 8:1211–1239. https://doi.org/10.5194/se-8-1211-2017

Vernon RH (ed) (2018) Microstructures of Deformed Rocks. In: A Practical Guide to Rock Microstructure, 2nd edn. Cambridge University Press, Cambridge, pp 228–352

Wawrzenitz N, Romer RL, Grasemann B, Morales LG (2019) Pre-UHP titanite archives pro- and retrograde episodes of fluid-marble-interaction (Dabie Shan UHP unit, China). Lithos 350–351:105232. https://doi.org/10.1016/j.lithos.2019.105232

Wayte GJ, Worden RH, Rubie DC, Droop GTR (1989) A TEM study of disequilibrium plagioclase breakdown at high pressure: the role of infiltrating fluid. Contrib Mineral Petrol 101:426–437. https://doi.org/10.1007/BF00372216

Wheeler J, Prior D, Jiang Z, et al (2001) The petrological significance of misorientations between grains. Contrib Mineral Petrol 141:109–124. https://doi.org/10.1007/s004100000225

White SH, Knipe RJ (1978) Transformation- and reaction-enhanced ductility in rocks. J Geol Soc 135:513–516. https://doi.org/10.1144/gsjgs.135.5.0513

Whitney DL, Evans BW (2010) Abbreviations for names of rock-forming minerals. Am Mineral 95:185–187. https://doi.org/10.2138/am.2010.3371

Wilke FDH, O'Brien PJ, Schmidt A, Ziemann MA (2015) Subduction, peak and multi-stage exhumation metamorphism: Traces from one coesite-bearing eclogite, Tso Morari, western Himalaya. Lithos 231:77–91. https://doi.org/10.1016/j.lithos.2015.06.007

Will TM, Schmädicke E (2001) A first find of retrogressed eclogites in the Odenwald Crystalline Complex, Mid-German Crystalline Rise, Germany: evidence for a so far unrecognised high-pressure metamorphism in the Central Variscides. Lithos 59:109–125. https://doi.org/10.1016/S0024-4937(01)00059-7

Wilson CJL (1975) Preferred Orientation in Quartz Ribbon Mylonites. GSA Bull 86:968–974. https://doi.org/10.1130/0016-7606(1975)86<968:POIQRM>2.0.CO;2

Wirth R, Kruhl JH, Morales LFG, Schreiber A (2022) Partially open grain and phase boundaries as fluid pathways in metamorphic and magmatic rocks. J Metamorph Geol 40:67–85. https://doi.org/10.1111/jmg.12610

Xia F, Brugger J, Ngothai Y, et al (2009) Three-Dimensional Ordered Arrays of Zeolite Nanocrystals with Uniform Size and Orientation by a Pseudomorphic Coupled Dissolution−Reprecipitation Replacement Route. Cryst Growth Des 9:4902–4906. https://doi.org/10.1021/cg900691a

Zertani S, Morales LFG, Menegon L (2024) Omphacite breakdown: nucleation and deformation of clinopyroxene-plagioclase symplectites. Contrib Mineral Petrol 179:44. https://doi.org/10.1007/s00410-024-02125-0

Zhang Z-M, Shen K, Sun W-D, et al (2008) Fluids in deeply subducted continental crust: Petrology, mineral chemistry and fluid inclusion of UHP metamorphic veins from the Sulu orogen, eastern China. Geochim Cosmochim Acta 72:3200–3228. https://doi.org/10.1016/j.gca.2008.04.014

Zhao S, Jin Z, Zhang J, et al (2012) Does subducting lithosphere weaken as it enters the lower mantle? Geophys Res Lett 39:. https://doi.org/10.1029/2012GL051666

Figure Captions

Fig. 1. Geological maps of the study area. **(a)** Geological map of the Himalayan orogen (reproduced from Dutta and Mukherjee, 2021). The yellow circles mark the locations of major cities/towns. The black triangles mark the major mountain peaks. The black unfilled square demarcates the study area. **(b)** Geological map of the Tso Morari region (redrawn after de Sigoyer et al., 2004 and Epard and Steck, 2008). White filled circles mark sample locations.

Fig. 2. Transmitted light photomicrographs and BSE images from the eclogite sample 17-6C. **(a)** Euhedral garnet porphyroblasts along with quartz and amphibole grains in the matrix (plane-polarized light). **(b)** Preferentially aligned, elliptical omphacite grains surrounded by symplectitic regions and matrix amphibole (plane-polarized light). **(c)** Omphacite grains in a matrix of quartz grains near a garnet porphyroblast in the eclogite. Retrograde amphibole grains are also present at the margin of the garnet porphyroblast. The omphacite grains are surrounded by symplectites (type S1), and most of them are fractured (yellow arrowheads). **(d)** Islands of partly symplectitised (type S1) omphacite within the amphibole matrix. **(e,f)** Cross-polarized photomicrographs of deformed quartz in the matrix with prominent subgrain boundaries (white arrowheads) and fluid inclusion trails (pink arrowheads). Migrated grain boundaries (blue arrowheads) are also visible. **(g)** Coarse and prismatic amphibole beside omphacite. **(h)** Coarse grains of white mica in the matrix alongside amphibole and garnet porphyroblast, with the latter containing inclusions of quartz. **(i)** Symplectitisation along the periphery of and across the omphacite grain. The thick bands of symplectite are nearly perpendicular to the long axis of the omphacites. The thinner linear stripes of coarse amphibole grains marked with the yellow arrows likely represent the original position of the fractures along which symplectitisation initiated. **(j)** The shapes of the former omphacite grains are preserved despite their complete replacement by symplectite (type S2). **(k)** Pervasive symplectitisation (type S2) with little trace of the precursor omphacites. **(l)** Zoomed-in image of **(i)** illustrating the gradual decrease in the amphibole grainsizes (yellow arrows) away from the initial position of the fracture. Mineral abbreviations are after Whitney and Evans (2010). The yellow arrowheads in **(c), (d),** and **(g)** point to the fractures.

Fig. 3. Transmitted light photomicrographs and BSE images of the garnet amphibolites. **(a)** Elongate amphibole grains surrounding a plagioclase-rich domain containing a fragment of a garnet porphyroblast. **(b)** An isolated patch of quartz-bearing plagioclase-rich domains containing garnet porphyroblasts. **(c)** Cross-polarized photomicrograph of a deformed quartz

grain with a prominent subgrain boundary (white arrowheads) surrounded by amphibole grains. **(d)** Prismatic amphibole grains define the foliation that warps around the garnet porphyroblast at the center (plane-polarized light). **(e)** Cross-polarized photomicrograph of a deformed quartz grain with visible subgrain boundaries (white arrowheads). **(f)** Amphibole-rich layers separated by quartz-bearing plagioclase-rich layers. **(a-c)** Sample 19-8B. **(d-f)** Sample 20-2.

Fig. 4. EPMA-derived amphibole mineral chemistry data from the eclogite and garnet amphibolite samples. Classification diagrams for calcic amphiboles **(a)** after Hawthorne et al. (2012) and **(b)** after Leake et al. (1997). Correlation plots of **(c)** Al_{total} (^{T}Al+^{C}Al) vs. $^{B}X_{Ca}$, **(d)** $^{C}(Al+Fe^{3+}+Ti)$ + $^{A}(Na+K)$ vs. ^{T}Al (Robinson et al. 1971), and **(e)** ^{T}Al v/s ^{B}Na (Brown 1977). Amp-S1 and Amp-S2 refer to the amphibole present in the two categories of symplectite, and Amp-M refers to the matrix amphibole (Sec. 4.2.1). Abbreviations-: Fe-Act: ferro-actinolite, Fe-Hbl: ferro-hornblende, Fe-Ts: ferri-tschermakite, and Mg-Hbl: magnesiohornblende. The rest of the mineral abbreviations are after Whitney and Evans (2010). Microprobe data of amphibole from the eclogites of the Western Gneiss Region (Norway) are also shown for easier comparison (Martin 2019). The mineral formula for this data is also recalculated based on 23 oxygens and 13 cations (excluding Ca, Na, K). The triangles and squares correspond to the amphibole of the symplectite and matrix around the garnet porphyroblasts, respectively. The degree of retrogression and amphibole content of the symplectites increases from sample 616-1 to 616-3 to 616-5.

Fig. 5. Phase maps, orientation (IPF-X) maps, and mineral CPOs from the symplectite regions of the eclogite sample 17-6C. **(a)**, **(e)**, and **(j)** are the phase maps for Site 1S, Site 1S-A, and Site 2S, respectively. **(b)**, **(f)**, and **(k)** are the orientation maps for Site 1S, Site 1S-A, and Site 2S, respectively. All orientation data points are plotted in the pole figures. Each data point in the pole figures is coded according to the orientation colour scheme (IPF key) of the corresponding mineral provided at the bottom left. The pole figures are presented as equal area, lower hemisphere projections (except for plagioclase, for which the upper hemisphere projections are also shown). The red diamonds at the peripheries of the pole figures mark the mean orientation of the omphacite grains. The ‘bilbao’ colormap of Crameri (2018) is used. n = number of orientation data points and M = misorientation index (Skemer et al. 2005).

Fig. 6. Phase maps, orientation (IPF-X) maps, and mineral CPOs from the matrix of the eclogite sample 17-6C. **(a)** phase map for Site 5M. **(b)** orientation map for Site 5M. The **(c)**

amphibole and **(d)** white mica pole figures are plotted following the *one-point-per-grain* scheme. The pole figures are presented as equal area, lower hemisphere projections. The 'bilbao' colormap of Crameri (2018) is used. n = number of orientation data points, N = number of grains, and M = misorientation index (Skemer et al. 2005).

Fig. 7. Phase maps, orientation maps, and mineral CPOs from the garnet amphibolite samples. **(a)** and **(e)** are the phase maps for samples 19-8B and 20-2, respectively. **(b)** and **(g)** are the orientation maps for samples 19-8B and 20-2, respectively. The *one-point-per-grain* pole figures of **(c,d)** 19-8B and **(g,h)** 20-2 are presented as equal area, lower hemisphere projections. They are contoured to multiples of uniform density when at least 50 grains are present. The 'bilbao' colormap of Crameri (2018) is used. The gray diamonds at the peripheries of the pole figures mark the mean orientation of the amphibole grains. N = number of grains and M = misorientation index (Skemer et al. 2005).

Fig. 8. Distributions of the low-angle (LAX, 2–<10°) and correlated high-angle (HAX, ≥10–160°) misorientation axes in crystal coordinate systems. Amphibole **(a)** LAXs and **(b,c)** HAXs from the symplectite Site 1S-A. Amphibole **(d)** LAXs and **(e)** HAXs from the symplectite Site 2S. Plagioclase **(f)** LAXs and **(g)** HAXs from the symplectite Site 1S-A. Plagioclase **(h)** LAXs and **(I,j)** HAXs from the symplectite Site 2S. The blue dots represent individual axis orientations, which are contoured to multiples of uniform density represented by the colorbars. The 'bilbao' colormap of Crameri (2018) is used. n = number of misorientation axes.

Fig. 9. Distributions of the low-angle (LAX, 2–<10°) and correlated high-angle (HAX, ≥10–160°) misorientation axes in crystal coordinate systems. LAXs of **(a)** amphibole and **(b)** quartz grains from the eclogite matrix. **(c)** LAXs and **(d,e)** HAXs of the amphibole grains from the garnet amphibolite sample 19-8B. **(f)** LAXs and **(g,h)** HAXs of the amphibole grains from the garnet amphibolite sample 20-2. The rest of the description is the same as that of Fig. 8.

Fig. 10. Misorientation angle distributions (MADs). **(a)** Amphibole and **(b)** plagioclase MADs from Site 1S-A of the eclogite sample 17-6C. **(c)** Amphibole and **(d)** plagioclase MADs from Site 2S of sample 17-6C. MADs of amphibole grains from the garnet amphibolite samples **(e)** 19-8B and **(f)** 20-2. The vertical bars represent the frequency distribution of the random-pair

misorientations. The neighbour-pair and theoretical misorientation angle distributions are represented by the red and dark green frequency curves.

Fig. 11. Misorientation (θ) to grain mean orientation (mis2mean) maps and misorientation profiles from the eclogite sample 17-6C. **(a)** mis2mean map of omphacite from Site 1S. **(b)** mis2mean map and **(c)** misorientation profile of one of the omphacite grains (red arrowhead in **(a)**). **(d)** mis2mean map of the omphacite from Site 1S-A. **(e)** mis2mean map and **(f)** misorientation profile of one of the grains (red arrowhead in **(d)**). The black arrowheads in the misorientation profiles point to the misorientation angle peaks corresponding to the subgrain boundaries. The 'lajolla' colormap of Crameri (2018) is used for all the mis2mean maps. Each colour bar represents the angular range of misorientation of the corresponding map/grain.

Fig. 12. Misorientation (θ) to grain mean orientation (mis2mean) maps and misorientation profiles of selected plagioclase grains from the eclogite sample 17-6C. **(a)** mis2mean map of plagioclase in the symplectite from Site 1S-A. **(b-d)** mis2mean maps of selected plagioclase grains (red arrowhead in **(a)**). Misorientation profiles along **(e)** A-B, **(f)** C-D, and **(E-F)** line segments in the plagioclase grains of **(b)**, **(c)**, and **(d)**, respectively. The rest of the description is the same as that of Fig. 11.

Fig. 13. Misorientation (θ) to grain mean orientation (mis2mean) maps and misorientation profiles of selected grains from the eclogite sample 17-6C. mis2mean map of **(a)** all amphibole grains and **(b)** one selected amphibole grain (red arrowhead in **(a)**) from the symplectite in Site 1S-A. **(c)** Misorientation profile along the A-B line segment in **(b)**. **(d)** mis2mean map of amphibole in the symplectite from Site 2S. **(e)** mis2mean map of a selected amphibole grain (red arrowhead in **(d)**). The misorientation profile along the line segments C-D is illustrated in **(f)**. **(g)** mis2mean map of amphibole from the matrix (Site 5M). **(h)** mis2mean map of a selected amphibole grain (red arrowhead in **(g)**). The misorientation profiles along the line segments E-F and G-H are illustrated in **(i)** and **(j)**, respectively. **(k)** mis2mean map of a quartz grain from the matrix (Site 7M). **(i)** illustrates the misorientation profiles along the line segment I-J. The rest of the description is the same as that of Fig. 11.

Fig. 14. Misorientation (θ) to grain mean orientation (mis2mean) maps and misorientation profiles of selected grains from the garnet amphibolites. **(a)** mis2mean map of amphibole from

the sample 19-8B. **(b)** and **(c)** are the misorientation profiles along the line segments A–B and C–D, respectively, marked in **(a)**. The mis2mean map of **(d)** all the amphibole grains and **(e,f)** two selected amphibole grains (red arrowheads in **(d)**) from the sample 20-2. **(g)** and **(h)** illustrate the misorientation profiles along the line segments **(e)** E–F and **(f)** G–H, respectively. The rest of the description is the same as that of Fig. 11.

Fig. 15. Schematic figure illustrating the sequential development of the two categories of symplectite in the studied eclogite. **(a)** Omphacite and quartz assemblage in the eclogite at or immediately after peak pressure. Progressive symplectitisation and development of **(b-d)** S1 and **(e-g)** S2 symplectites. Greater supply of hydrous fluids generated more amphibole grains in the latter case. The relatively thinner peripheries of the omphacite grains in **(b-d)** than in **(e-g)** also represent the availability of more hydrous fluids in the latter. **(h)** and **(i)** show magnified illustrations of the omphacite-symplectite interfaces for the S1 and S2 symplectites, respectively. An additional Stage IV can be visualized for the S1 and S2 symplectites as reduced size and disappearance, respectively, of the omphacite grains.